17th Brazilian Congress of Thermal Sciences and Engineering
November 25th-28th, 2018, Águas de Lindóia, SP, Brazil

ENCIT-2018-0195
NUMERICAL AND EXPERIMENTAL CHARACTERIZATION OF SUBSONIC FLOW AROUND A CIRCULAR CYLINDER: WIND TUNNEL MEASUREMENT CAPABILITIES AND TURBULENCE MODELS SUITABILITY.

Leonardo Flores Tymchuk
Cesar Celis
Mechanical Engineering Section, Pontificia Universidad Católica del Perú
Av. Universitaria 1801, San Miguel, Lima 32, Lima, Peru
leonardo.flores@pucp.pe
ccelis@pucp.edu.pe

Armando Blanco Alvarez
Department of Mechanics, Universidad Simón Bolivar
Sartenejas, Baruta, Edo. Miranda - Apartado 89000 Cable Unibolivar, Caracas, Venezuela
ajblanco@usb.ve

Abstract. *Through a detailed numerical and experimental characterization of subsonic flow around a circular cylinder, the measurement capabilities of a wind tunnel are assessed in this work. More specifically, computational fluid dynamics (CFD) results are used to determine the flow range in which the wind tunnel produces accurate results, given the current limitations of the instrumentation available in the wind tunnel. The influence of three turbulence models, namely shear-stress transport (SST) k-ω, Transition SST and Scale-Adaptive Simulation (SAS), on the obtained numerical results, is analyzed as well. For the numerical computations, a range of Reynolds numbers from 10 to* $1.4x10^5$ *is covered accounting for subsonic and incompressible flow. For the experimental analysis in turn, a Reynolds number range up to* $1.2x10^5$ *is studied in the wind tunnel. Aiming to reduce the associated computational cost, several simulation strategies taking into account different solution methods, under-relaxation factors and time discretization schemes are studied as well. The influence of turbulence models on the obtained numerical results is qualitatively analyzed considering contours of velocity, vorticity, shear layers, transition to turbulence, among others. In quantitative terms, the referred influence is discussed accounting for drag, lift and pressure coefficients, as well as for the boundary layer separation angle. Variations of key parameters as a function of Reynolds number and along their frequencies spectra are properly discussed as well. A relative good agreement is noticed between the wind tunnel measurements and experimental measurements from the literature. A relative good agreement between the numerical results obtained here for the laminar regime and those associated with similar studies carried out in the past is observed as well. Nonetheless, larger discrepancies were found at turbulent regimes between the numerical simulations and experimental measurements from this work and literature. The results from this work will be used in future to specify new and more sophisticated instrumentation to be installed in the particular wind tunnel analyzed here.*

Keywords: *Circular cylinder, computational fluid dynamics, measurements, wind tunnel*

1. INTRODUCTION

Conducting highly specialized research requires a continuous upgrade in instrumentation and computational resources. Because the processing capacity of computers increases continuously, the capability for carrying out numerical simulations increases as well. This allows, for instance, simulating wider Reynolds number-related flow ranges nowadays. Besides, experimentation becomes gradually more sophisticated than ever and the instrumentation utilized is much more powerful every time. Sophisticated measurement techniques include, for instance, laser Doppler velocimetry (LDV) (Molki *et al.*, 2013), laser-induced incandescence (LII) (Leipertz and Sommer, 2009), volumetric velocimetry (TOMO PIV) (Hegner *et al.*, 2015) and laser-induced fluorescence (LIF) (Lobasov *et al.*, 2017). It is important therefore to assess the instrumentation available in a test rig to determine the operating limits in which measurements are reliable.

In literature, there are a number of works dealing with computational fluid dynamics (CFD) based simulations and circular cylinders. For instance, two-dimensional unsteady Reynolds Averaged Navier-Stokes (RANS) calculations

using a *k-ω* SST turbulence model and the viscous-flow solver ReFRESCO were performed by Rosetti *et al.* (2012). Strict verification and validation (V&V) procedures along with assessments of numerical errors and uncertainties were performed in the referred work. Discrepancies between their numerical results and experimental data were attributed to modeling errors. The ReFRESCO flow solver was further explored by Pereira *et al.* (2016) through the analysis of transitional flow at a Reynolds number of $1.4x10^5$. In this last work, different modeling approaches were considered such as RANS, Scale-Adaptive Simulation (SAS), Delayed Detached-Eddy Simulation (DDES), eXtra Large-Eddy Simulation (XLES) and Partially-Averaged Navier-Stokes (PANS). This comparison showed that in transitional flows models based on RANS boundary-layer solvers predict incorrectly the flow separation. Nevertheless, approaches that solve turbulence on the boundary-layer such as PANS present better results. A comparison between a commercial and an open-source solver results was performed by Stringer *et al.* (2014). Six different Reynolds numbers ranging from 40 to 10^6 were considered and a *k-ω* SST turbulence model was used in both solvers with the same geometry and mesh. Despite the similar configurations set up on both solvers, several differences were found in the results. The commercial code turned out to be more suitable in high Reynolds numbers for drag, lift and Strouhal number computations, while the open-source solver had a better agreement in low Reynolds numbers for the same computed parameters. LES and unsteady RANS based results for two and three-dimensional flows were assessed against experimental data by Young and Ooi (2007) for a Reynolds number of 3900. A standard *k-ω* model was used for the unsteady RANS computations and a dynamic Smagorinsky sub-grid scale model was used for the LES approach. The CPU-time was also registered there, where the three dimensional LES computations took about 1784 CPU-hours, much higher than the 17 CPU-hours associated with the two-dimensional unsteady RANS ones. The results from the three-dimensional LES case with 48 spanwise cells accurately reproduced experimental results for drag, lift and base pressure coefficients, as well as for Strouhal numbers. LES cases with lower spanwise cells showed poor results, which suggested that LES is only effective when used with enough cells in the spanwise direction to be able to solve the smaller three-dimensional eddies. The Reynolds number equal to 3,900, which is interesting to study because of its flow characteristics (laminar boundary layer, laminar separation, transition to turbulent at the near-wake and turbulent wake) was also studied by Pereira *et al.* (2015). In the referred work, hybrid models such as DDES and XLES were compared with RANS simulations, and a better agreement with experimental data was found for the hybrid models. To unravel the widespread perception that RANS simulations fail to adequately represent separated flows, Palkin *et al.* (2016) performed simulations over a three-dimensional circular cylinder with a Reynolds stress model (RSM) and a linear eddy-viscosity model (LEVM). The results for two Reynolds numbers, $3.9x10^3$ and $1.4x10^5$, were compared with experimental data, LES and direct numerical simulations (DNS). Good agreement with LES was gathered by RSM for high Reynolds numbers. Nevertheless, for low Reynolds numbers, the unsteady RANS models did not result reliable for fully separated flows.

Similarly, several experimental works involving circular cylinders and wind tunnels have been performed in the past. Achenbach (1968) made measurements of the pressure coefficient (C_P) and the friction coefficient (C_F). From the friction coefficient, the boundary layer separation angle (θ_S) was calculated. Cantwell and Coles (1983) performed a shedding frequency and vortex formation analysis in the cylinder near wake and downstream regions. Norberg (2003) performed a transient analysis of lift coefficients (C_L). Roshko (1961) performed an analysis of the pressure distribution for very high Reynolds numbers. Williamson (1996) conducted a study of vortex formation in the wake of a cylinder, as well as of frequency spectrum as a function of Reynolds number. The referred experimental works are widely used in different research efforts and can be therefore accepted as trustable validation resources. More recently, for instance, a methodology for wind tunnel experiments is proposed by Libii (2011). This last work describes procedures to study fluctuations in a free flow stream, pressure distributions around a circular cylinder and viscous wake width behind a circular cylinder. Most of the experiments carried out there were performed measuring pressure with a pressure probe and estimating the flow velocity from those measurements. Experimental studies at a Reynolds number Re = 3900 with hot-wire anemometry (HWA) and particle image velocimetry (PIV) were performed by Parnaudeau *et al.* (2008). In this last study near wake ($x/D < 3$) and further downstream ($3 < x/D < 10$) analyses were carried out. The agreement between their experimental results and LES calculations performed was satisfactory. The results of these works are taken into account here as a reference for the measurements carried out in this work.

In order to make a fair comparison between numerical and experimental procedures, the capabilities of the measuring instruments must be determined with precision. There are three basic instruments for measuring punctual flow velocities, (i) the Pitot tube, (ii) hot-wire anemometer and (iii) laser-Doppler anemometer (Tritton, 1988/2007). Regarding the Pitot tube, it is remarked that a high Reynolds number is required so that the theory of non-viscous fluid could be applied and the pressure could be related to the velocity by the Bernoulli equation. Pitot tube main limitations are its large size and its high time response for fast pressure variations. It is concluded then that for turbulent flows with a Pitot tube is possible to measure *average* velocities only. In contrast, the hot-wire anemometer is relatively small and capable of measuring high frequencies in transition and turbulent regimes. Its main limitations are the need to keep the instrument always calibrated and free of problems associated with the presence of temperature variations. Finally, the laser-Doppler anemometer measures the velocity of small particles that travel with the instantaneous flow velocity. The laser-Doppler has a wide range of speeds that can be measured and it is able to measure values under $1\mu ms^{-1}$. It also responds to rapid fluctuations in velocity so it is suitable to measure transitional and turbulent flows. Its main

drawbacks are the complex installation in some experimental conditions and the presence of many sources of inaccuracies.

In this work, the measurement capabilities of a wind tunnel are evaluated via a detailed characterization of subsonic flow around a circular cylinder compared with numerical simulations. Initially, CFD based results for wind-tunnel conditions are compared with experimental data available in open literature. Once the accuracy of the numerical model is assured, a comparison between numerical predictions and experimental measures was done. The referred results are then used to determine the flow range in which the wind tunnel produces accurate results, given the current limitations of the instrumentation available in the wind tunnel. For the numerical computations, a range of Reynolds numbers from 10 to $1.4x10^5$ is covered accounting for subsonic and incompressible flow. For the experimental analysis in turn, a Reynolds number range up to $1.2x10^5$ is studied in the wind tunnel. In order to reduce the associated computational cost, several simulation strategies taking account different simulation methods, under-relaxation factors and time discretization schemes are studied as well. The influence on the numerical results of the mesh refinement is also analyzed considering the dimensionless parameter Y^+ and the number of cells in the cylinder perimeter. The influence of three turbulence models, shear-stress transport (SST) k-ω, Transition SST and Scale-Adaptive Simulation (SAS), on the obtained numerical results is analyzed qualitatively and quantitatively. Qualitatively, comparisons of contours of velocity, vorticity, shear layers, transition to turbulence, among others, are performed. In quantitative terms, analyses of drag, lift and pressure coefficients are carried out. Finally, variations of different parameters such as force and pressure coefficients, Strouhal number and boundary layer detachment angles as a function of Reynolds number are also discussed.

Accordingly, after a brief introduction (Section 1), the governing equations and mathematical models employed in this work are summarized in Section 2. Section 3 describes in turn the experimental and numerical methodology followed here. The description and discussion of the main results obtained in this work are presented in Section 4. Finally, the last sections include the main conclusions drawn from these results.

2. MATHEMATICAL MODELING

2.1. Governing equations

The conservative form of the system of equations governing the time-dependent two-dimensional flow of an incompressible and isothermal fluid is accounted for this work. An index notation with *i* and *j* indexes is used here where x_i *(i = 1, 2)*, or *(x, y)*, are the Cartesian coordinates and u_i *(i=1, 2)*, or *(u, v)*, are the Cartesian components of the velocity vector. Mass and momentum conservation are therefore expressed as, respectively (Ferziger and Peric, 2002),

$$\frac{\partial u_i}{\partial x_i} = 0, \tag{1}$$

$$\frac{\partial u_i}{\partial t} + \frac{\partial (u_j u_i)}{\partial x_j} = -\frac{1}{\rho}\frac{\partial p}{\partial x_i} + \frac{\mu}{\rho}\frac{\partial}{\partial x_j}\left(\frac{\partial u_i}{\partial x_j} + \frac{\partial u_j}{\partial x_i}\right) + s_{u_i}, \tag{2}$$

where ρ stands for density, μ is dynamic viscosity, p is pressure and s_{u_i} is a source term. Different approaches to solve these instantaneous equations such as RANS, LES, DNS and hybrid as Detached Eddy Simulation (DES) are available.

2.2. Reynolds Averaged Navier-Stokes (RANS) formulation

The equations solved in this work are based on the RANS formulation, which is the less computational demanding approach. Following this approach, Eqs. (1) and (2) are written as, respectively (Ferziger and Peric, 2002),

$$\frac{\partial \overline{u}_i}{\partial x_i} = 0, \tag{3}$$

$$\frac{\partial (\overline{u}_i)}{\partial t} + \frac{\partial}{\partial x_j}\left(\overline{u}_i \overline{u}_j + \overline{u_i' u_j'}\right) = -\frac{1}{\rho}\frac{\partial \bar{p}}{\partial x_i} + \frac{\mu}{\rho}\frac{\partial}{\partial x_j}\left(\frac{\partial \overline{u}_i}{\partial x_j} + \frac{\partial \overline{u}_j}{\partial x_i}\right). \tag{4}$$

The Eqs. (3) and (4) terms come from accounting for the dependent variables u_i and p as $u_i = \overline{u}_i + u_i'$ and $p = \bar{p} + p$, respectively. Here $\overline{u}_i$ and $\bar{p}$ are the mean values of u_i and p, and u_i' and p' are their fluctuating components. As it can be noticed, the averaging process introduces extra variables, $\overline{u_i' u_j'}$, known as Reynolds stresses. This means that for solving these equations further modeling is required.

2.3. Turbulence modeling

The Boussinesq approximation, Eq. (5), expresses the Reynolds stresses in terms of turbulent viscosity μ_t, mean rates of deformation and turbulent kinetic energy k (Ferziger and Peric, 2002),

$$\tau_{ij} = -\rho\overline{u_i{}'u_j{}'} = \mu_t\left(\frac{\partial\overline{u}_i}{\partial x_j}+\frac{\partial\overline{u}_j}{\partial x_i}\right)-\frac{2}{3}\rho k\delta_{ij}, \tag{5}$$

where $k=\sqrt{\overline{u'^2}+\overline{v'^2}}$. The Boussinesq approximation implies an isotropic assumption for the normal Reynolds stresses, which means that the turbulent viscosity is considered to be the same in all directions. Its main application is in two-equation turbulence models like k-ε or k-ω. Thus, expressions for modeling the turbulent viscosity and the turbulent kinetic energy are required. As described next, three turbulence models have been studied in this work. In the following, for the sake of simplicity, the mean values are redefined by dropping the over bar.

2.3.1 Menter shear-stress transport (SST) k-ω model

This hybrid model, involving the k-ε (Jones and Launder, 1972) and k-ω (Wilcox, 1988) turbulence models, was originally developed by Menter (1994). In this model, the best features of the Wilcox k-ω model in the near-wall region and of the k-ε model in the free-stream region are combined. The transport equations, Eq. (6) and (7), for k and ω are given by, respectively (Menter, 2003),

$$\frac{\partial(k)}{\partial t}+\frac{\partial\left(ku_j\right)}{\partial x_j}=\frac{\partial}{\partial x_j}\left[\left(\frac{\mu}{\rho}+\frac{\mu_t}{\rho\sigma_k}\right)\frac{\partial k}{\partial x_j}\right]+min(\mu_t S^2,10\beta^*\omega k)-\beta^* k\omega, \tag{6}$$

$$\frac{\partial(\omega)}{\partial t}+\frac{\partial\left(\omega u_j\right)}{\partial x_j}=\frac{\partial}{\partial x_j}\left[\left(\frac{\mu}{\rho}+\frac{\mu_t}{\rho\sigma_\omega}\right)\frac{\partial\omega}{\partial x_j}\right]+\frac{\alpha}{\mu_t}min(\mu_t S^2,10\beta^*\omega k)-\beta\omega^2+2(1-F_1)\frac{1}{\sigma_{\omega 2}}\frac{1}{\omega}\frac{\partial k}{\partial x_j}\frac{\partial\omega}{\partial x_j}, \tag{7}$$

where σ_k and σ_ω are the turbulent Prandtl numbers for k and ω, respectively, which depend on the wall distance; S is the magnitude of the strain rate $S=\sqrt{2S_{ij}S_{ij}}$; S_{ij} is the strain rate tensor $S_{ij}=0.5\left(\partial u_i/\partial x_j+\partial u_j/\partial x_i\right)$; β^* is a function that depends on the Reynolds number; α and β are functions that relate k-ε and k-ω constants; F_1 is a blending function which is zero away from the surface and one in the near-wall region and $\sigma_{\omega 2}$ is a constant. A production limiter, denoted by the *min* function of the turbulence production term in the k-equation, is used to avoid the overproduction of turbulence in stagnation points. Over the years the terms $\beta^*$and β_i have been modified from the original Menter's equation to be Reynolds number dependable.

Notice that in this model the turbulent viscosity μ_t present in the diffusive terms is obtained from,

$$\mu_t=\frac{\rho k}{\omega}\frac{1}{\max(1;\frac{SF_2}{a_1\omega})}, \tag{8}$$

where F_2 is a second blending function and a_1 is a constant. Default model configurations and constants were utilized in this work, as recommended by the commercial solver utilized (ANSYS® Fluent, 2017a).

2.3.2. Transition SST model

This model is based on the coupling of the Menter's SST k-ω model with two other transport equations. The first one is the intermittency γ, Eq. (9), which is the parameter responsible of triggering the transition process. And the second one is the transition momentum-thickness Reynolds number $\widetilde{Re}_{\theta t}$, Eq. (10), which is used to capture the non-local effect of free-stream turbulence intensity and pressure gradient at the boundary layer edge (Menter, 2006),

$$\frac{\partial(\gamma)}{\partial t}+\frac{\partial\left(\gamma u_j\right)}{\partial x_j}=\frac{\partial}{\partial x_j}\left[\left(\frac{\mu}{\rho}+\frac{\mu_t}{\rho\sigma_\gamma}\right)\frac{\partial\gamma}{\partial x_j}\right]+C_{a1}F_{length}S[\gamma F_{onset}]^{c_{\gamma 3}}\left[1-\frac{C_{e1}\gamma}{\rho}\right]+C_{a2}\Omega F_{turb}\left[1-\frac{C_{e2}\gamma}{\rho}\right], \tag{9}$$

$$\frac{\partial(\widetilde{Re}_{\theta t})}{\partial t}+\frac{\partial\left(\widetilde{Re}_{\theta t}u_j\right)}{\partial x_j}=\frac{\partial}{\partial x_j}\left[\sigma_{\theta t}\left(\frac{\mu+\mu_t}{\rho}\right)\frac{\partial\widetilde{Re}_{\theta t}}{\partial x_j}\right]+c_{\theta t}\frac{1}{t}\left(Re_{\theta t}-\widetilde{Re}_{\theta t}\right)(1-F_{\theta t}). \tag{10}$$

Here σ_γ, C_{a1}, $c_{\gamma 3}$, C_{e1}, C_{a2}, C_{e2}, $\sigma_{\theta t}$, $c_{\theta t}$ are model constants; F_{length}, $Re_{\theta t}$ are empirical correlations given by Langtry and Menter (2009), F_{onset} is a function that controls the transition onset; Ω is the vorticity magnitude $\Omega = \sqrt{2\Omega_{ij}\Omega_{ij}}$; Ω_{ij} is the mean rate-of-rotation tensor $\Omega_{ij} = 0.5\left(\partial u_i/\partial x_j - \partial u_j/\partial x_i\right)$; F_{turb} is a function used to disable the destruction/relaminarization sources outside of a laminar boundary layer or in the viscous sublayer; t is a time scale included for dimensional reasons and $F_{\theta t}$ is a blending function used to turn off the source term in the boundary layer and to allow the transported scalar $\widetilde{Re}_{\theta t}$ diffusing in from the freestream (Menter, 2006).

A separation-induced transition correction is also considered in this model to avoid the transition effect because of the boundary layer separation. It allows the local intermittency to exceed 1 whenever the boundary layer separates. This causes an earlier reattachment by increasing the production of *k*. The corresponding equation is given by (Menter, 2006),

$$\gamma_{sep} = min\left\{C_{s1} max\left[\left(\frac{Re_v}{3235 Re_{\theta c}}\right) - 1{,}0\right] F_{reattach}, 2\right\} F_{\theta t}, \tag{11}$$

where C_{s1} is a constant that controls the separation bubble, Re_v is the strain rate Reynolds Number, $F_{reattach}$ is a function that disables the correction when the viscosity ratio is high enough to cause reattachment and $Re_{\theta c}$ is an empirical correlation that defines where the intermittency starts to increase in the boundary layer.

The coupling of the two additional transport equations with the Menter *k-ω* SST model modifies the *k* equation as follows (Menter, 2006),

$$\frac{\partial(k)}{\partial t} + \frac{\partial\left(k u_j\right)}{\partial x_j} = \frac{\partial}{\partial x_j}\left[\left(\frac{\mu}{\rho} + \frac{\mu_t}{\rho\sigma_k}\right)\frac{\partial k}{\partial x_j}\right] + \gamma_{eff} min(\mu_t S\Omega, 10\beta^*\omega k) - \min(\max\left(\gamma_{eff}, 0.1\right), 1)\beta^* k\omega, \tag{12}$$

where γ_{eff} is the effective intermittency $\gamma_{eff} = \max(\gamma, \gamma_{sep})$. The last modification concerning the original F_1 blending function and further details of the model are provided in Langtry and Menter (2009). Also, a turbulence energy production limiter Kato-Launder, denoted as $\mu_t S\Omega$ instead of $\mu_t S^2$, is considered by default by the solver utilized to reduce the kinetic energy production in the stagnation regions (ANSYS® Fluent, 2017a).

2.3.3. Scale Adaptive Simulation (SAS) model

The SAS model is an improved URANS model which models different turbulent scales without the need of filtering the Navier Stokes equations as the LES approach does. This model is based on the introduction of the von Karman length-scale into the turbulent scale equation, Eq. (7), as a source term. This model differs from other two-equation models focus, in the way that in classical two-equation models only one scale of turbulence is calculated (for instance, the turbulent frequency *ω*, proportional to the Strain Rate *S*, in the case of the models based on the *k-ω* equations) and the maximum turbulent length scale *L* will be always proportional to the thickness of the turbulent layer δ_t. This approach is valid for steady shear flows, but in unsteady conditions, where instabilities occur, different length scales tend to appear. In the classical approach, since they have the same turbulent frequency, different scale eddies tend to merge in one unique large eddy. This aspect can be noticed in the *k-ω* SST and transition SST models result obtained in this work (Section 4.2). So, using higher derivatives in the source terms, different Strain Rates *S* can be achieved in the domain (Menter and Egorov, 2010). The source term Q_{SAS} used is defined by,

$$Q_{SAS} = max\left[\rho\eta_2\kappa S^2\left(\frac{L}{L_{vK}}\right)^2 - C_{SAS}\frac{2\rho k}{\sigma_\Phi}\max\left(\frac{1}{k^2}\frac{\partial k}{\partial x_j}\frac{\partial k}{\partial x_j}, \frac{1}{\omega^2}\frac{\partial\omega}{\partial x_j}\frac{\partial\omega}{\partial x_j}\right), 0\right], \tag{13}$$

where η_2, κ, C_{SAS} and σ_Φ are constants, L is the length scale of the modeled turbulence and L_{vK} is the von Kármán length scale. This term is added as an additional source term in the right side of the *ω* transport equation, Eq. (7). In this work the source term Q_{SAS} is considered as an extension of the transition SST model. The terms appearing in Eq. (13) are defined as described in ANSYS® Fluent (2017a) and are equivalent to those proposed by Menter and Egorov (2010).

3. METHODOLOGY

Both numerical and experimental methodologies followed in this work are described in this section.

3.1. Numerical methodology

To manage the different steps of the simulation process, such as the creation of geometry, mesh generation, setup, solver monitoring and post-processing, the ANSYS® Workbench 19.0 (ANSYS® Workbench, 2017) commercial

software was used as a versatile platform to distribute the grids, cases and data generated through different processes. In particular, the numerical simulations were carried out using the commercial solver ANSYS® Fluent 19.0 (ANSYS® Fluent, 2017b). The geometric configuration was defined accounting for the computational domains considered in similar studies (Franke and Frank, 2002; Parnaudeau *et al*., 2008; Rosetti *et al*., 2012). The geometry of the circular cylinder studied was obtained from the physical model available for experimentation. More specifically, a computational domain of 30*D* long and 20*D* wide, with a circular cylinder of 72.6 mm diameter (*D*), placed at a distance of 10D from the inlet, was simulated in this work. Computational grids were generated following a multi-block approach using ANSYS® ICEM CFD 19.0 (ANSYS® ICEM CFD, 2017). Figure 1 shows the structured mesh of $1.6x10^5$ elements utilized. Fluid properties, such as air density and dynamic viscosity, were determined considering the atmospheric pressure, temperature and humidity of the wind tunnel studied. The domain inlet boundary condition was considered as velocity-inlet with a constant velocity vector in the x-direction. A turbulent intensity of 0.5%, which corresponds to that specified by the wind tunnel manufacturer, was considered at the inlet to maintain the similarity with the experiments. Also, a turbulence length scale of 5mm, 7% of the characteristic length (ANSYS® Fluent, 2017a), was considered at the inlet. The outlet boundary condition was set up as pressure-outlet with a zero gauge pressure. The upper and lower boundaries were set up as walls with zero shear stress values (slip condition). The initialization of the domain was carried out with a hybrid configuration, which is a set of recipes and boundary interpolation methods that improve the initial calculations (ANSYS® Fluent, 2017a).

Globally scaled residuals were considered for all the simulations, with a scaled residual of 10^{-5} for the unsteady cases and 10^{-10} for the steady cases. The drag coefficient (C_D) and the lift coefficient (C_L) are integral values of the pressure field around the cylinder wall. The boundary-layer separation angle (Θ_S) is computed from the wall shear stress at the cylinder. This is when it changes of sign from positive to negative. The base suction coefficient ($-C_{PB}$) is an indicator of the behavior of the vortices shedding (Williamson, 1996) and is calculated as the static pressure at the rear of the cylinder wall. The velocity at the outlet (V_{OUT}) is the *x*-velocity at the midpoint of the outlet boundary and is an indicator of the domain convergence. From the temporal variations of C_L, the vortex shedding frequencies and the Strouhal number (St) were derived with a fast Fourier transform (FFT) algorithm. Also, data sampling for time statistics was performed during the last 50 non-dimensional time units of the unsteady simulations to obtain time-averaged fields comparable with experimental data.

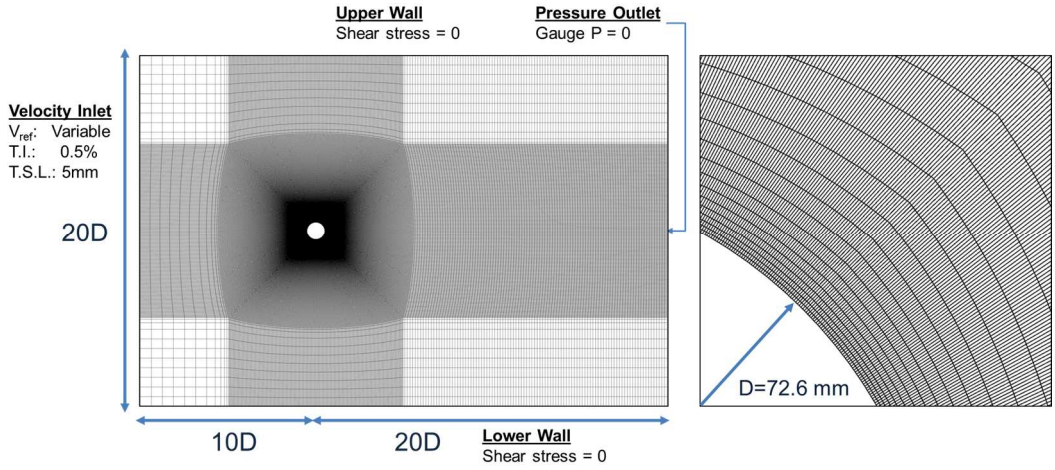

Figure 1. Left: Computational domain and details of the mesh utilized (162,342 cells). Right: Zoomed view of the mesh resolution around the cylinder.

3.2. Experimental methodology

To carry out the experimental tests, a subsonic wind tunnel, Figure 2, belonging to the Laboratory of Energy (LABEN) at the Pontificia Universidad Católica del Peru (PUCP) was utilized. The blower tunnel features a maximum air speed of 30.5 m/s according to the manufacturer specifications. The air speed of the tunnel was originally controlled by a throttle valve on the fan inlet. Later modifications involved the installation of an electric motor controller, so the throttle valve is now left completely open and the revolutions per minute (RPM) of the electric motor are adjusted through a control panel. The tunnel's available instrumentation for the interest of this work includes a Pitot tube, a low frequencies Delta Ohm hot-wire anemometer HD 2103.2 with a resolution of 0.01 m/s, a TecQuipment AFA3 three-component balance, two TecQuipment AFA5 differential pressure transducers with a range of 1 to 7000 Pa with a resolution of 1 Pa and a TecQuipment VDAS-F (mkII) module allowing real-time data acquisition with a maximum digital sampling frequency of 2 Hz. Higher frequencies can be monitored and stored via an analogical input properly

configured. The software used to store and manage the data is VDAS® (TecQuipment, 2017), which includes an integrated interface to manage all the instruments used in the wind tunnel.

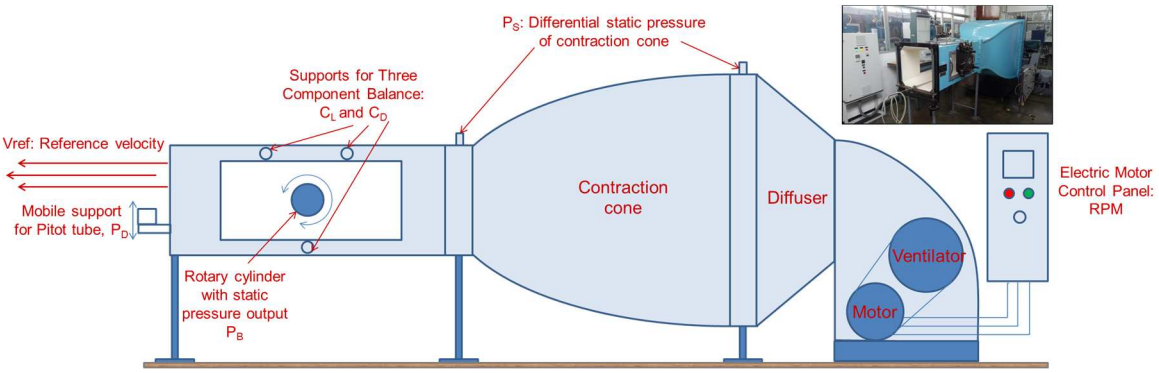

Figure 2. Scheme of the wind tunnel of the LABEN describing the sources of the input parameter RPM and output parameters P_B, P_D, P_S, C_L and C_D.

From the instruments available, the three-component balance was used to obtain the drag and lift coefficients. For the balance related measurements, a continuous data collection of drag and lift forces was carried out varying the tunnel mean flow velocity at the highest sampling frequency. At the same time, the base suction pressure was obtained at the rear point of the cylinder, $\theta=180°$. Figure 3 shows the cylinder angles distribution accounted for velocity-based of the flow direction. The differential pressure transducers were used to measure the Pitot tube dynamic pressure. The Pitot tube experiments were done by locating the Pitot tube at the location of interest inside the working section and measuring continuous data at the highest sampling frequency, as the velocity was varied. The static pressure around the cylinder was measured by varying the position angle of the static pressure intake θ maintaining a constant flow velocity. In parallel, the differential static pressure between the inlet and outlet of the tunnel's contraction cone was always monitored and registered during the experiments to have a reference of the flow mean velocity. Correction factors defined by Allen and Vincenti (1944) and used by many other authors (Roshko, 1961) were also considered here for correcting the drag and pressure coefficients due to the blockage ratio between the cylinder and the wind tunnel working section height (BR=0.159).

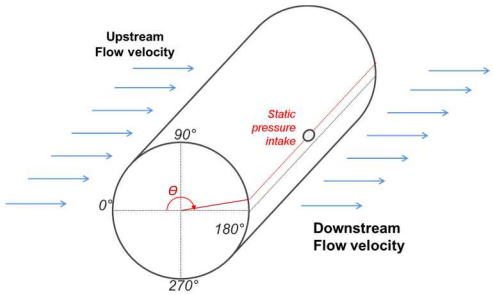

Figure 3. Scheme of the circular cylinder angles with respect to the flow direction and static pressure intake.

A verification of the wind tunnel velocity was performed prior to the experimentation to get a general idea of the wind tunnel capabilities and calibration factors. A relationship between the Pitot tube dynamic pressure P_D and the velocity $V_{Pitot} = \sqrt{P_D/(0.5\rho)}$ and a relationship for the pressure at the contraction cone P_s and the velocity $V_{cont.cone} = \sqrt{P_s/\left(0.5\rho(1-(A_2/A_1)^2)\right)}$, where A_2/A_1 is the area ratio of the contraction cone equal to 0.158, were defined. Both equations were defined considering the Bernoulli equation and the continuity equation for a steady flow. Then, by setting up a relationship between the rotational speed of the electric motor (RPM) and the free stream velocity of the wind tunnel obtained with the hot-wire anemometer, calibration factors were defined for V_{Pitot} and $V_{cont.cone}$. Thus, by monitoring the differential pressure of the contraction cone, accurate free-stream flow velocity could be measured. Figure 4 shows the relationship between the RPM and the Reynolds number, as well as the flow velocities obtained from the hot-wire anemometer, the calibrated Pitot tube and the calibrated contraction cone as a function of the Reynolds number. The maximum velocity reached by the wind tunnel was 23.1 m/s. This means that a maximum Reynolds number based on the cylinder diameter of about $1.1\text{x}10^5$ can be achieved. Due to overcharging risks and high currents consumption only short tests were carried out at the maximum flow velocity. On the other hand, a minimum V_{ref} of 7.7 m/s, corresponding to a Reynolds number of around 37,000, is considered as acceptable for measurement.

This accounts for the minimum resolution of the differential pressure transducers of 1 Pa. Lower velocities measured with the Pitot tube drastically increase the measurement uncertainties. In the working range, a flow velocity average fluctuation of 1.4% was obtained following the procedure suggested by Libii (2011), which was an indicator of the low-turbulence characteristics of the wind tunnel.

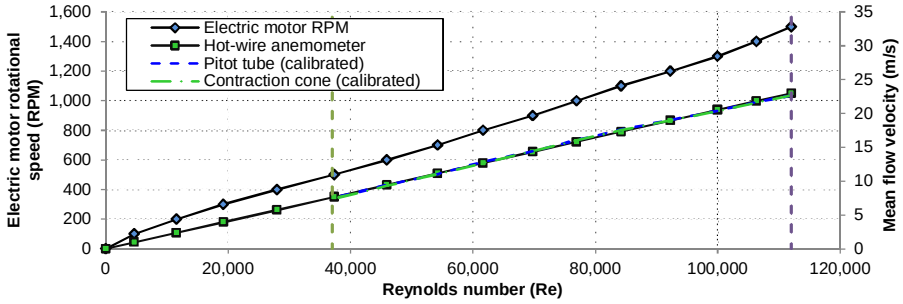

Figure 4. Left axis: (-◊-) Electric motor rotational speed. Right axis: (-■-) Wind tunnel mean flow velocity measured with a hot-wire anemometer, (---) corrected flow velocity measured with the Pitot tube and (-·-) corrected flow velocity measured at the contraction cone. All as a function of Reynolds number.

4. RESULTS

A set of eight different Reynolds numbers ranging from 10 to $1.4x10^5$ were simulated numerically and a Reynolds number range from $3.7x10^4$ to $1.2x10^5$ was studied experimentally by the variation of the free-stream velocity. Reynolds numbers of 10 and 40 are expected to show characteristics of steady laminar flow, where a crescent recirculation bubble is expected to appear for the higher value. Re = 100 and 200 are expected to show laminar unsteady characteristics such as the Von Karman vortex street, as a result of instabilities in the recirculation length. Despite Zdravkovich (1990) and Williamson (1996) define the beginning of turbulence effects around Reynolds numbers of 150-300, in this work is considered that Reynolds number of 200 is still laminar, as considered by Rosetti *et al.* (2012). Three-dimensional effects start to appear around Re = 260 (Williamson, 1996), where dislocations along the spanwise should cause a reduction of the base suction coefficient ($-C_{PB}$) and an increase of the formation region. Nevertheless, a two-dimensional approach is considered here during the numerical simulations, so the absence of three-dimensional effects needs to be taken into account. Three different turbulent models where considered for the Reynolds numbers 1,000, 3,900, 40,000 and 140,000, which are inside of the subcritical regime (Williamson, 1996). This is where transitional effects from laminar to turbulent are expected to occur in the free shear layer. From these Reynolds numbers, Re = 1,000 and 3,900 are both in the TrSL2 sub-regime defined by Zdravkovich (1990), where transitional vortices are expected in the shear layer. The highest Reynolds numbers numerically analyzed, Re = 40,000 and 140,000, as well as the experimental range, are part of the TrSL3 sub-regime, where the shear layer is expected to behave fully turbulent from the beginning. Table 1 summarizes the 16 different cases numerically studied in this work.

Table 1. Summary of cases numerically simulated.

Case	Re	V m/s	Model	y^+	Δs (mm)
1	10	0.00215	laminar Steady	-	0.300
2	40	0.00860	laminar Steady	-	0.300
3	100	0.0215	laminar Unsteady	-	0.300
4	200	0.0430	laminar Unsteady	-	0.300
5			k-ω SST		
6	3,900	0.839	Transition SST	1.02	0.300
7			SAS		
8			k-ω SST		
9	10,000	2.15	Transition SST	0.98	0.120
10			SAS		
11			k-ω SST		
12	40,000	8.60	Transition SST	1.00	0.034
13			SAS		
14			k-ω SST		
15	140,000	30.1	Transition SST	0.94	0.010
16			SAS		

4.1. Preliminary results

Several preliminary tests involving studies of grid independence and simulation strategies were initially performed.

4.1.2. Mesh independence

A set of seven different grids were created in order to evaluate how the domain spatial discretization affects the numerical results. A constant flow velocity corresponding to a Reynolds number of $1.4x10^5$ was evaluated. This Reynolds number is the critical one studied in this work since it is the maximum possible value to be gathered according to the wind tunnel manufacturer specifications. Notice that this *Re* value is lower than the upper limit defining the subcritical regime related range (Raghavan and Bernitsas, 2011). A constant Y^+ of 0.94 was kept in all simulations so the viscous sub-layer could be solved and Y^+ independence could be achieved (ANSYS® Fluent, 2017a). The *k-ω* SST turbulence model is considered in this set of mesh independence related simulations. Since all the turbulence models used in this work are based on the Wilcox *k-ω* model, it seems reasonable to assume that the achieved grid independence will be valid for the transitional SST and SAS turbulence models as well. Accordingly, Table 2 summarizes the mean values obtained for the C_D, $-C_{PB}$ and θ_S, as well as the amplitudes of the unsteady behavior of the C_D, C_L and $-C_{PB}$, and the Strouhal number. Figure 5 illustrates the variations of some of these parameters with respect to the grid refinement. Note that mean values for the lift coefficient C_L were not considered since all of them are around zero.

Table 2. Mesh and flow characteristic parameters

No	Total mesh cells	Circunf. Cells	Mean C_D	C_D Amplitude	C_L Amplitude	Mean $-C_{PB}$	$-C_{PB}$ Amplitude	St	Mean θ_S
1	9,888	318	0.921	0.201	2.33	1.24	0.770	0.246	76.2
2	41,228	650	0.861	0.142	1.96	1.09	0.568	0.248	78.7
3	91,074	966	0.850	0.130	1.87	1.06	0.520	0.250	79.1
4	162,342	1,289	0.844	0.123	1.81	1.04	0.490	0.253	79.2
5	248,928	1,597	0.849	0.125	1.82	1.05	0.493	0.256	79.1
6	354,820	1,906	0.856	0.130	1.84	1.06	0.509	0.259	79.1
7	498,074	2,258	0.869	0.140	1.91	1.09	0.546	0.262	78.9

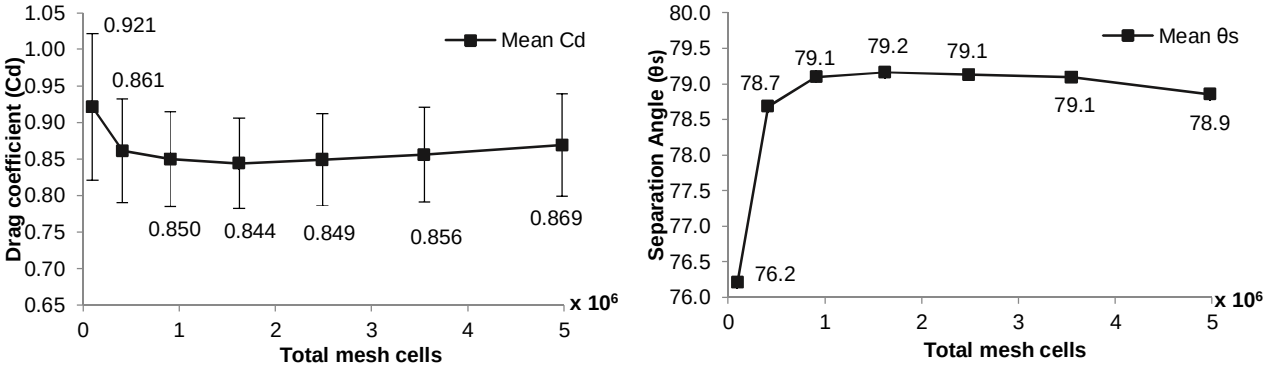

Figure 5. Left: Mean drag coefficient and amplitude (vertical bars). Right: Mean boundary layer separation angle. Both graphics are plotted as a function of total domain mesh cells.

From the obtained results, grid independent ones were considered for the fourth mesh, which features 162,342 total cells and 1,289 circumferential cells. In forms of results, the discrepancies of this mesh with the finest one accounted for here are about 3% for the drag coefficient, 5% for the lift coefficient and 2% for the Strouhal number. Considering that these differences are acceptable, and due to the significant computational cost associated with the most refined mesh, the fourth mesh was considered for the numerical studies carried out in this work.

4.1.3. Simulation strategies

Strong dependence between CPU-time and spatial discretization was noticed during the grid independence related simulations. Since several simplifications are considered in this work such as two-dimensional domain, RANS

equations, incompressible and subcritical flow, there is a particular interest in analyzing different simulation strategies by monitoring CPU and wall-clock times. Different iterative and non-iterative solution methods were thus compared for a Reynolds number of 3,900. Time-step variations, from coarse to fine, were also performed during some calculations. The non-iterative methods were found to be the less CPU-demanding methods. The Courant-Friedrich-Lewi (CFL) number was considered as an indicator of time-discretization and stability. Accordingly, several simulation strategies for steady and unsteady state situations were analyzed.

Developing a simulation strategy for steady state cases is important when considering the solution of Reynolds numbers below 49, where the laminar steady flow is developed (Williamson, 1996). Moreover, steady solutions are important as well because they represent a good initialization for unsteady simulations due to its lower CPU-time cost. Table 3 details the results obtained from steady state simulations using segregated methods (SIMPLE and SIMPLEC), where pressure and momentum equations are solved separately; and coupled methods, where pressure and momentum equations are solved together. It was noticed that segregated methods have a tendency to diverge, which seems reasonable because of the unsteady nature of the flow at higher Reynolds numbers. On the other hand, the computations based on coupled methods do converge and take fewer iterations but consume more CPU-time to do so. Nevertheless, the coupled pseudo-transient method shows the best results since it only requires 120 iterations while the others methods need more than 1400 iterations to achieve residuals convergence (when possible). The CPU cost is in this case much lower than the others and computed parameters are very similar to those obtained using the coupled method.

Table 3. Steady state simulation methods comparison for a Re = 3,900.

No	Solution Method	Convergence	Max. Absolute Residual	Total Iterations	CPU Time (s)	Mean C_D	Mean C_L	Mean $-C_{PB}$
1	SIMPLE	Diverged	2.8E-04	2000	3122	0.757	-0.077	0.377
2	SIMPLEC	Diverged	8.9E-04	2000	3125	0.757	-0.079	0.377
3	Coupled	Converged	1.0E-05	1455	4356	0.809	0.000	0.537
4	Coupled Pseudo-Transient	Converged	1.0E-05	120	554	0.811	0.000	0.540

Unsteady state simulations present additional complexities due to their fluctuating characteristics. One of them is their convergence criteria. Since the velocity field and pressure distribution are continually changing, the residuals monitoring is not a good convergence indicator, as in the steady state related simulations. A way to realize if the field has converged is observing the nature of the solution. For instance, alternating shedding of vortices in unsteady RANS cross flows tends to behave with a given frequency and amplitude. Thus, velocity, pressure and integral variables such as the lift coefficient can be considered as converged when their alternating amplitude and frequency behavior is stabilized (present constant values). For convergence purposes, in the comparison of the different simulation strategies studied, the velocity in the center of the domain outlet V_{out} was considered in this work. The convergence criterion for each time step was based on globally scaled residuals of $1x10^{-5}$ for each transport equation. Iterative methods, such as SIMPLE, PISO and coupled, were compared with the non-iterative time advanced (NITA) method fractional step and the numerical results are shown in Figure 6 while the main results are summarized in Table 4. Contrary to what one could expect, the unsteady simulation initialized with a steady field (option 2 from Table 4), presents a higher CPU cost than that using a hybrid initialization only (option 1). It seems that the steady-converged field reaches the unsteady state in more time than in the case of unsteady initialization because the convergence criterion ($1x10^{5}$) is fulfilled from the beginning in fewer iterations. The PISO method (option 3) seems less attractive because of its high CPU cost, resulting from the extra steps for skewness and neighbor corrections carried in this method, which does not seem necessary for the type of flow analyzed here. Although the coupled method (option 4) has a lower computational cost, it does not show great improvements. Besides, this method consumes a large amount of memory because it solves both pressure and momentum equations at the same time. Lower computational costs were found varying CFL numbers during the simulation (option 5 and 6). However, the most cost-effective method resulted to be the NITA fractional step (option 7), with a computational cost of about ten times less than the iterative methods. Because an under-relaxation factor equal to 1 (associated with the update of the computed variables for all the equations solved) has been considered for the fractional step method, high Courant numbers tend to diverge easily. The best simulation strategy found without affecting the numerical accuracy is the fractional step method with variable time step size (option 8). Variations of time steps are made automatically in this work using solver macros. This means that the change is made in a specific time step without the need to configure it manually.

Table 4. Unsteady state strategies comparison for a Re = 3,900. Default under-relaxation factors utilized. Calculations performed using double-precision and four computer nodes.

Option	Method (Initialization)	CFL Number	Time-Steps.	Total Iterations	Wall-clock time (s)	CPU Time (s)	C_D Avg	C_L Amp	$-C_{PB}$ Avg
1	SIMPLE (Unsteady)	5	7000	157235	61576	288844	1.64	3.36	1.93
2	SIMPLE (Steady)	5	10000	179162	69133	312904	1.64	3.36	1.94
3	PISO (Steady)	5	10000	202008	91212	397995	1.64	3.34	1.93
4	Coupled (Steady)	5	10000	90436	63252	281912	1.63	3.33	1.93
5	SIMPLE (Unsteady)	625→125→25→5	3500	149055	64806	287939	1.64	3.35	1.93
6	SIMPLE (Steady)	625→125→25→5	3620	112532	41814	192064	1.64	3.36	1.94
7	NITA Fractional Step (Unsteady)	5	7000	-	6999	37414	1.63	3.37	1.92
8	NITA Fractional Step (Unsteady)	25→5	4500	-	4112	24280	1.63	3.37	1.91

Further insights about the simulation strategies accounted for can be obtained by analyzing the time trace results shown in Figure 7, which presents a comparison of the convergence behavior considering a non-dimensional time $t^* = tV_{ref}/D$. It can be noticed from this figure that in the simulations starting from a steady state, the steady behavior is strong until almost 100 time units and seems to be responsible for its high CPU cost. On the other hand, unsteady state simulations have a peak from the beginning and have a fluctuating behavior throughout all the time, which seems to help reach its stabilization in about half the time. In this work thus, a fractional step approach was utilized for the most CPU-demanding cases such as the turbulent models comparison at Re = 140,000 and all the Reynolds numbers with the SAS model. For the other cases simulated here a SIMPLE method starting from an unsteady state was considered. A second order spatial discretization and a bounded second order implicit transient formulation was used for all the cases.

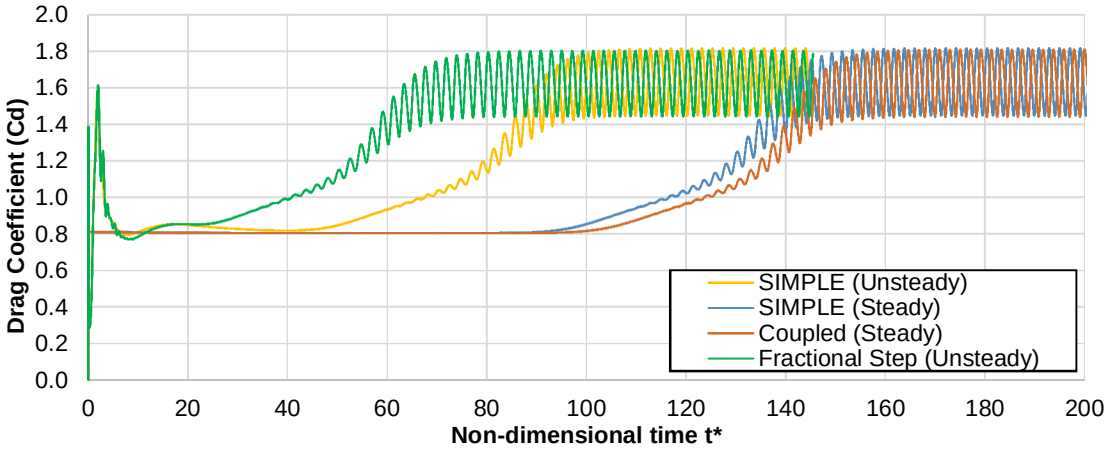

Figure 6. Time trace comparison of unsteady state simulation strategies for a Re = 3900.

4.2 Qualitative analyses

Qualitative results such as contours, streamlines and vector fields are a good way to characterize the behavior of a flow. In experimentation, this kind of information can be gathered through flow visualization techniques such as direct injection of smoke and particle image velocimetry (PIV) (Ristić, 2007). Since instruments related to visualization techniques are not available in the LABEN, significant information was gathered through numerical simulations. This includes velocity fields comparison considering different laminar Reynolds numbers and an assessment of different turbulence models.

4.2.1 Laminar regime

Figure 7 shows the normalized *x*-velocity contours for laminar steady (*Re*=10 and 40) and unsteady (Re = 100 and 200) regimes. A symmetrical velocity field can be observed in the steady regimen, as it is expected in flows below 49 (Williamson, 1996). Also, a larger recirculation bubble, denoted by the negative x-velocity values, is observed to increase in the near wake region of the cylinder as the Re increases from 10 to 40. Unsteady effects are also visualized in Figure 7, where velocity periodic fluctuations are showed at the particular time step when C_L is maximum. It is worth noticing from these plots that, for a Re = 200, higher velocities tend to be more pronounced at the cylinder wake and its width tend to be narrower in comparison to Re=100.

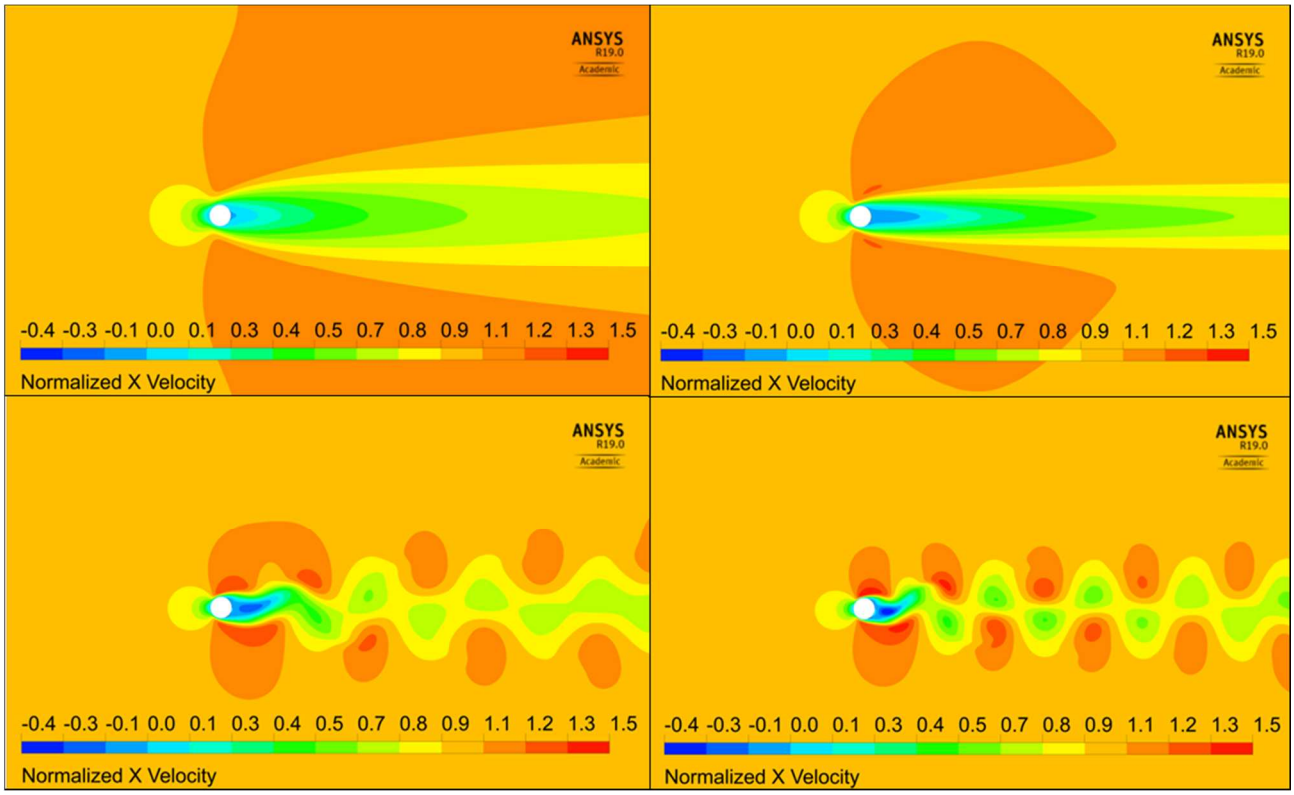

Figure 7. Top left and right plots, Re = 10 and 40, respectively: contours of instantaneous normalized *x*-velocity (V = V/V_{REF}) for the converged solution. Bottom left and right plots, Re=100 and 200, respectively: contours of instantaneous normalized *x*-velocity when the lift coefficient is maximum.

4.2.2 Turbulent regime

For the analysis of turbulence characteristics, the highest Reynolds number assessed in this work (Re=140k) was accounted for. The vorticity field is a good indicator of the vortex shedding. Thus, Figure 8 shows periodic eddies, where the red and blue fields denote the clockwise and counter-clockwise rotating eddies, respectively. Similar vorticity contours can be observed in Figure 8 between the k-ω SST and the transition SST model since the transition model only affects the near wall regions. Nonetheless, the k-ω SST model shows more vortices at the wake than the transition SST model, which is an indicator of a higher shedding frequency. Secondary vortices at the near wall region can be observed for the three turbulent models. The small secondary vortices tend to merge with the biggest scale eddies for the k-ω SST and the transition SST models. Nevertheless, different vortices-scales are visualized at the wake of the SAS model. This behavior appears to be more realistic since different scales with different frequencies are observed. Moreover, the SAS model shows larger differences in comparison of the k-ω SST and transition SST models, where the vorticity caused by the vortex shedding is not periodically arranged anymore.

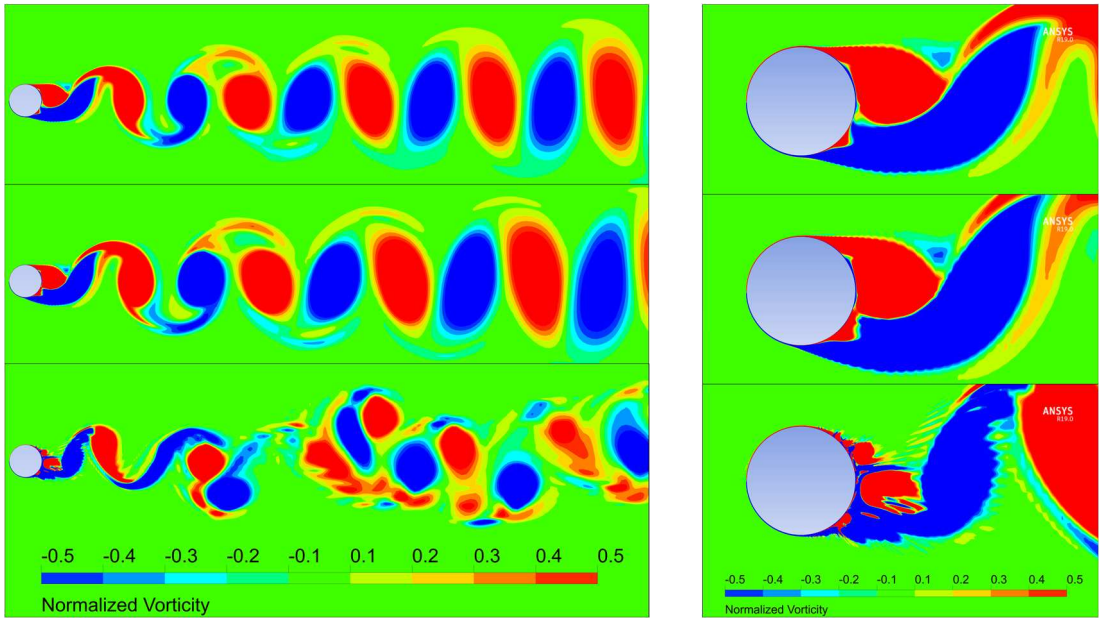

Figure 8. Full domain contours (left plots) and zoomed (right plots) of instantaneous normalized vorticity when the lift coefficient is maximum. Top plots: k-ω SST model. Middle plots: Transition SST model. Bottom plots: SAS model.

The turbulent viscosity ratio, as it is shown in Figure 9, is a good indicator of the transition between the laminar and turbulent regimes. The free-stream region (green field) shows a constant turbulent viscosity ratio. Below the free stream region, low turbulent viscosity ratios are observed near the wall regions. Higher values of this ratio (yellow and red) denote a high turbulent viscosity, which indicates that the field is completely turbulent. The computed near wall regions are very different for each turbulence model. At the cylinder upstream region, the k-ω SST model shows high viscosity ratios, while the transition SST shows a gross laminar region, where the air dynamic viscosity plays a key role. The SAS model shows an intermediate behavior between the k-ω SST and transitional SST models at the upstream region. The SAS model seems to be characterized by low values of turbulent viscosity ratio at the upstream region and laminar regions going further downstream of the flow. Since this Reynolds number Re = 140,000 is a characterized by a fully turbulent free shear layer and wake, it can be said in advance that the SAS model does not capture properly the near wake region.

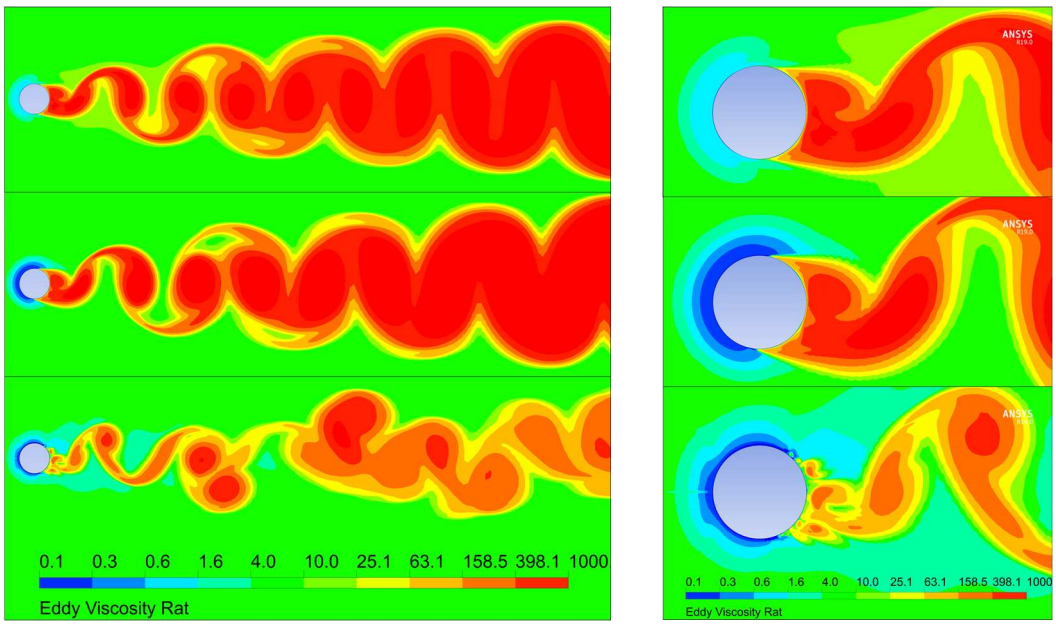

Figure 9. Contours of instantaneous turbulent viscosity ratio when the lift coefficient is maximum. Top: k-ω SST model. Middle plots: Transition SST model. Bottom plots: SAS model. The contours scale is logarithmic.

4.2.3. Transition to turbulence.

The four turbulent Reynolds numbers considered in this work are within the subcritical flow regimen. The subcritical regimen has been extensively characterized in literature and has very marked regions such as a laminar boundary layer, laminar separation, transition to turbulent flow in the shear layer and completely turbulent wake (Williamson, 1996). Moreover, Zdravkovich (1990) classifies the subcritical regimen into three different regimens. The first one, denoted by TrSL1, and ranged from Re = 350-500 to 1,000-2000, is characterized by the development of transition waves in the free shear layer. The second regimen, called TrSL2 and ranged from Re = 1,000-2,000 to 20,000-40,000 is characterized by the formation of transition vortices in the free shear layer and the third one, characterized by a fully turbulent shear layer, TrSL3, between Re = 20,000-40,000 to 100,000 to 200,000.

The Figure 10 shows basically three important characteristics of the flow around the cylinder. The first one is the boundary layer, represented as an iso-line at a velocity equal to the 99 percent of the free-stream velocity. The second one is the separation of the boundary layer (BL), represented as an iso-line where the *x*-velocity is equal to zero. And the third one is the differentiation of the laminar and the turbulent regions, where the laminar region can be estimated as the region where the turbulent viscosity ratio μ/μ_t is less than 1, the low turbulence region between 25 and 100 and the fully turbulent region as more than 100. Following this considerations, it can be said that the k-ω SST model fails to represent the subcritical regime in a Reynolds number of 40,000 and 140,000 because the BL separation occurs in the transitional region (white). On the other hand, the transition SST responds accurately to the TrSL3 characteristics at the same Reynolds numbers. For instance, the boundary layer separation occurs in the laminar region (blue), the transition begins just after the BL separation and the transition in the free shear layer results to be completely turbulent. The SAS model accomplishes the laminar separation, but does not seem to have a fully turbulent free shear layer, neither a fully turbulent wake region. Although the results obtained for Re = 3,900 and 10,000 are not shown in this work, the three turbulence models show similar characteristics for each Reynolds number. Moreover, the k-ω SST achieves the expected characteristics for a TrSL2 regime, where transition can be observed in the free shear layer. The similarities between these characteristics explain the similar results of C_D, C_L, $-C_{PB}$, St and separation angle obtained. This implies that there is no need to use the more complex models such as Transition SST and SAS in low Re transition regimes and a k-ω SST model suffices for these regimes.

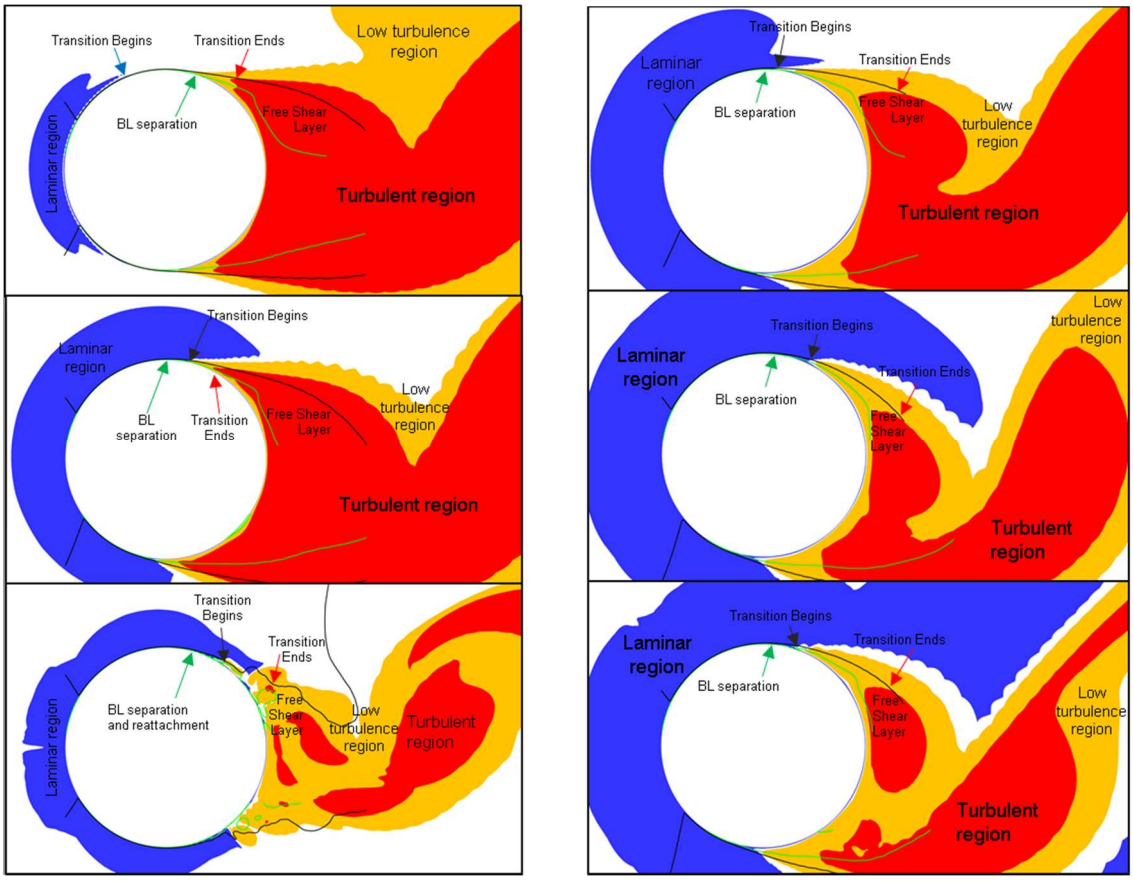

Figure 10. Details of the transition from laminar to turbulent corresponding to the TrSL3 regime. Re = 140, 000 (left) and Re = 40,000 (right). Blue contour: laminar region. Red contour: turbulent region. Black iso-line: external boundary layer (BL) and shear layer limit Green iso-line: zero x-velocity.

4.3. Quantitative analyses

Besides carrying out qualitative analyzes, it is important to compare the numerical results quantitatively, computing for instance parameters such as the drag and lift coefficients. Integral parameters such as drag need also to be verified by analyzing the pressure distribution around the wall of the cylinder. Table 5 shows a comparison of numerical and experimental results for the different Reynolds numbers corresponding to the laminar and turbulent regimes analyzed in this work. The turbulent models show similar results at each Reynolds number up to 10,000. Several differences between the turbulent model's simulations and the wind tunnel measurements are noticed at Reynolds numbers 40,000 and 140,000.

Table 5. Comparison of numerical and experimental results for different Reynolds numbers.

Re	Model	C_D Avg.	C_L rms	- C_{PB} Avg.	St	θ_S
10	laminar Steady	3.03	-	0.686	-	150.9
40	laminar Steady	1.61	-	0.493	-	126.9
100	laminar Unsteady	1.38	0.226	0.686	0.166	116.8
200	laminar Unsteady	1.38	0.490	0.951	0.199	111.8
3,900	k-ω SST	1.64	1.19	1.93	0.241	98.4
	Transition SST	1.60	1.17	1.85	0.231	98.4
	SAS	1.64	1.23	1.91	0.223	100.9
10,000	k-ω SST	1.74	1.34	2.13	0.244	99.0
	Transition SST	1.71	1.33	2.07	0.234	98.1
	SAS	1.70	1.32	2.00	0.247	99.7
40,000	Wind Tunnel	0.96	-	0.93	-	80
	k-ω SST	1.16	0.848	1.39	0.237	88.6
	Transition SST	1.70	1.47	2.08	0.230	95.4
	SAS	1.64	1.36	1.92	0.208	93.7
120,000	Wind Tunnel	1.06	-	1.04	-	-
140,000	k-ω SST	0.84	0.631	1.04	0.251	100.8
	Transition SST	1.15	0.997	1.48	0.217	88.2
	SAS	0.43	0.451	0.471	0.309	98.7

4.3.1. Pressure distribution around the cylinder.

Force parameters such as lift and drag coefficients depend directly on the pressure and friction distribution around the cylinder wall. For Reynolds numbers within the TrSL2 sub-regime the effects of the viscosity are very low, and for higher Re the viscous effects are null (Zdravkovich, 1990). Thus, in such conditions, the viscous effects can be neglected and the turbulent flow regimes can be considered as being influenced by pressure effects only. Therefore, plotting the pressure distribution around the cylinder let to verify if the lift and drag values obtained from the numerical simulations are consistent with those obtained experimentally.

A comparison between experimental and numerical pressure distribution at a Re = 40,000 was carried on. Experimentally, the pressure distribution was measured every 5 and 10 degrees, depending on the region of interest, and 40 data points were measured at each angle to obtain the pressure fluctuations. Numerically, the static pressure coefficient was obtained from the time-averaged pressure field. Figure 11 shows a comparison between the potential flow, the experimental measurements and the turbulence models simulated. A normalization of the results was made to coincide the numerical and experimental values with the potential flow at the zero angles. It is clear from the figure that the potential flow does not represent adequately the pressure distribution. On the other hand, numerical simulations have a quite similar tendency to the actual experimental values. All three turbulence models follow a very similar tendency to the experimental values up to 60°. From 60 to around 90 degrees all the models underestimate the experimental minimum pressure, although the SAS model shows better agreement with experimental measurements by Weidman (1968). After 90° a negative slope of the pressure coefficient is noticed in the wind tunnel measurements and in Weidman (1968) measurements. From 120° to 180° the k-ω SST model seems to fit in the experimental measurements. It can be noticed that the experimental measurements in the wind tunnel were able to capture the slight pressure drop around 180°, which is highly underestimated by the transition SST and SAS models. By this comparison, it can be noticed that the simulated models do not represent adequately the whole experimental distribution around the cylinder wall.

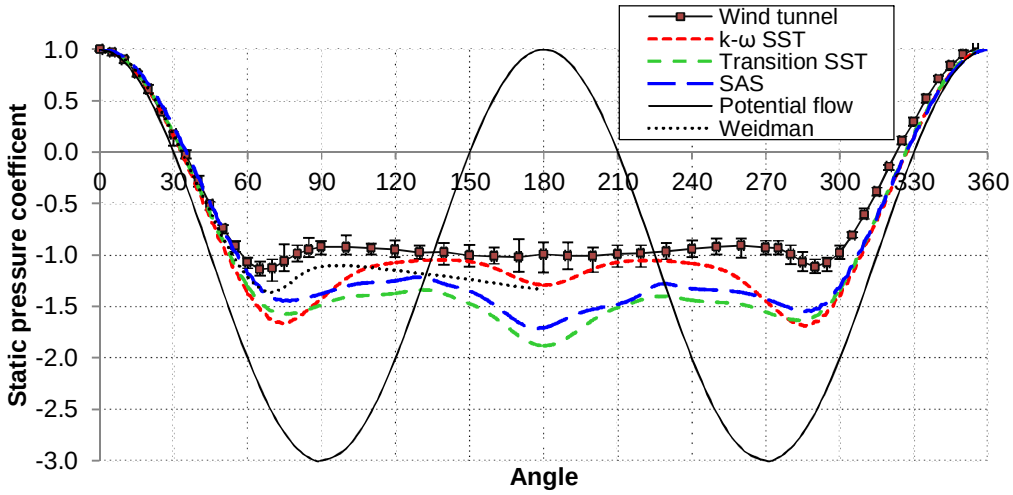

Figure 11. Distribution of pressure coefficient C_P around the cylinder for Re=40 000 (Normalized to C_P=1.0 at 0°). (■) present wind tunnel measurements; (----) present work, k-ω SST turbulence model; (−−−) present work, transition SST turbulence model; (▬ ▬) present work, SAS model; (▬) potential flow; (···) experiment of Weidman (1968) for Re = 43,000.

4.3.2. Velocity distribution at the cylinder wake

Another indicator of the flow behavior can be obtained through the analysis of the wake. Data was measured every 5 or 10 mm in the *y*-direction behind the cylinder at a distance of 1.1 and 3 diameters. A total of 20 data points were measured at each point to obtain the velocity fluctuations. For the numerical simulations, a line was drawn at a distance of 1.1 and 3 diameters behind the cylinder, and a time-averaged *x*-velocity field was calculated at the lines. Figure 12 shows a comparison of the wind tunnel measurements and the three turbulence models considered.

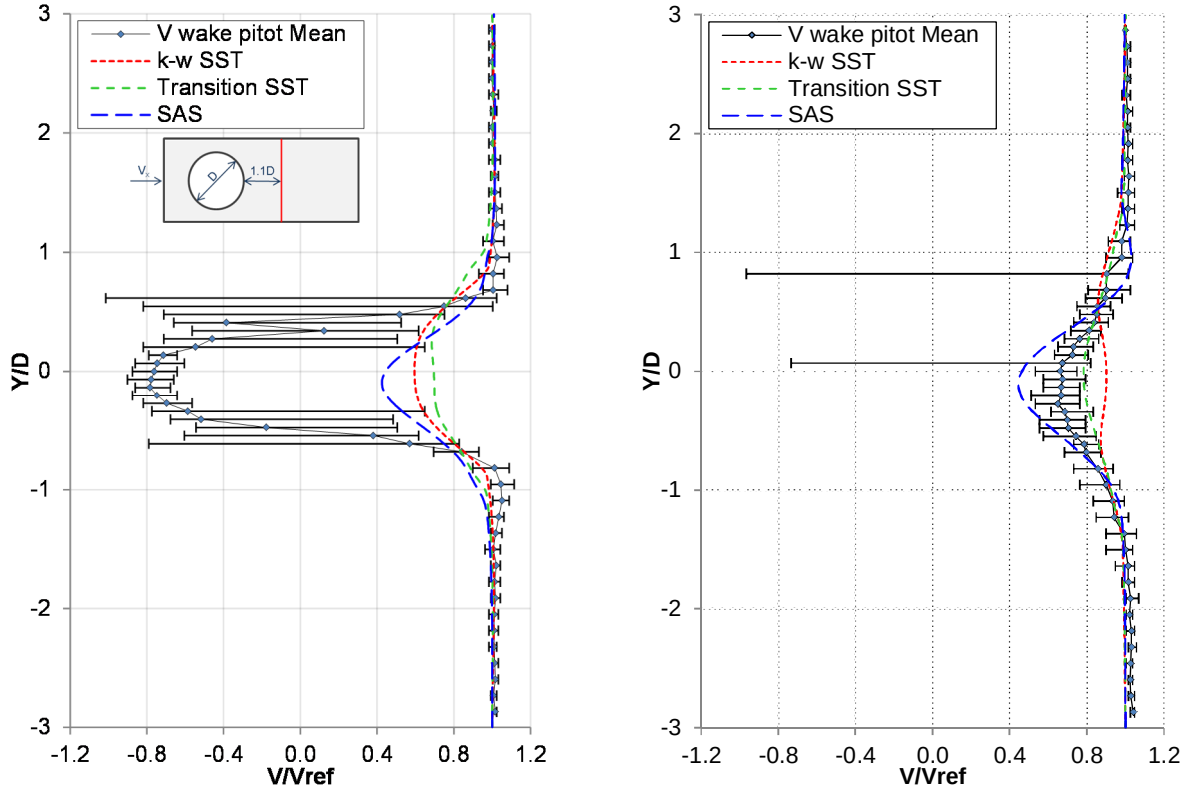

Figure 12. *x*-velocity distribution at the wake of the cylinder at distance of *x*=1.1D and *x*=3D. The horizontal bars show the maximum and minimum velocity fluctuations at each point. (Normalized to *V/Vref* = 1 at *y/D* = 3). (◊) present wind tunnel measurements; (---) k-ω SST turbulence model; (−−−) transition SST turbulence model; (▬ ▬) SAS model

A normalization of the free-stream velocity from the experimentation and the free-stream from the simulation was made for V/V_{REF} = 1 at a distance of *y=3D*. The free stream velocity measured was about 13% higher than the free stream velocity expected at a distance of *1.1D* and 6% at a distance of *3D*. This means that the cylinder confinement in the wind tunnel caused a free stream velocity increment around the cylinder because of the sectional area reduction. As the measurements are further from the cylinder (x = 3D case), the free stream velocity tends to be equal to the reference flow velocity. The Figure 12 left plot shows that the numerical models fail to represent the recirculation zone (negative velocities at the wake) in the near-wake region of the cylinder. Nevertheless, the experimental data achieves to represent adequately the slight velocity increase ($V/V_{REF} > 1$) in the same plot at y/D = 1 and -1. The U-shape of the velocity profile is also captured by the present experimental measurements (Parnaudeau *et al.*, 2008). Further experimentation at the near wake region (x=1.1D) should consider the presence of the velocity drops at a distance of y/D=0.5 and -0.5. The last mentioned effect could be an indicator of the turbulent free shear layer. In the wake region of the cylinder (x=3*D)*, the transition SST model represents better the external region up to y=-0.5 and 0.5 but underestimates the velocity in the internal region. The SAS model shows an increase ($V/V_{REF} > 1$) at a distance of y/D=1, which is more characteristic in near-wake regions. The SAS model also overpredicts the velocity behind the cylinder. Pressure drops were noted in the further wake region at a distance of y/D=0.1 and 0.8 approximately, which could be caused by low-pressure regions at the wake.

4.3.3. Time traces and Strouhal number

The time evolution of monitored parameters shows the unsteady characteristics of the flow. For instance, the k-ω SST and transition SST models time traces show in Figure 13 a periodic behavior with an apparent constant amplitude. For these models, the frequency spectrum shows that only one Strouhal frequency is dominant. Higher harmonic frequencies, three times the main one, are noticed by considering a smaller power spectral density scale. This refutes Rosetti *et al*. (2012) who notes harmonics of twice the main frequency. The harmonics can be related to secondary vortices at the near wall regions of the cylinder, which periodically appear and tend to disappear at the near wake, primarily by the convection and merge with larger eddies with smaller frequencies (Braza *et al*., 1986). Power Spectral Density is related to the amplitude of the signal as PSD = $A^2/(3\Delta f)$, where Δf is the frequency resolution. The SAS model shows a non-periodic behavior with different amplitudes for all the monitored parameters. This is evidenced by the Strouhal frequency spectrum, where one dominant frequency with *St* = 0.309 and three secondary lower frequencies with *St* = 0.0245, 0.0678 and 0.111 are apparent. The lower frequencies of the SAS model can be noted in the time traces, where the mean signal has a wave behavior. Two higher frequencies appear in the SAS model as well, with a Strouhal frequency of 0.505 and 0.563. These high frequencies are related to secondary vortices. Further spectral analysis at the wake could be of special interest to evaluate the development of the secondary eddies considering different turbulence models. Considering all the cases, large amplitudes can be noticed, especially for the lift coefficient in Figure 13. This effect was noted by Young and Ooi (2007) as well, where three-dimensional simulations with few spanwise cells showed large amplitudes of drag and lift coefficients. These amplitudes were diminished when the spanwise resolution was increased. By this, the three-dimensional analysis is recommended to be considered in further assessments.

4.3.4. Effects of Reynolds number on C_D, $-C_{PB}$, St and θ_S.

The numerical results obtained show a good agreement with data obtained in similar studies (Rosetti *et al*., 2012), but show several disparities with literature experimental data at the turbulent regimes. The experimental results obtained in this work have an acceptable agreement with literature data, nevertheless, only represent a fraction of the complete range analyzed in this work. Figure 14, Figure 15, Figure 16 and Figure 17 show drag coefficients C_D, base suction coefficients $-C_{PB}$, Strouhal numbers *St* and separation angles θ_S, respectively. Notice how the disagreement of the numerical data with literature experimental data starts around Re=260, the point where three-dimensional effects start to appear (Williamson, 1996). The laminar steady and unsteady regimen of the drag coefficient, from Figure 14, show that the numerical results follow relatively well the trends characterizing the literature experimental data (Schlichting and Gersten, 2017). The laminar Re = 10 where a 10% deviation is noticed may be caused by discrepancies between different experimental measurements. For turbulent Reynolds numbers, a good qualitative approach is found but several discrepancies between the numerical results and the experimental data appear. Firstly, all the drag coefficients obtained by the models differ from the literature experimental information. Although the Re=40,000 k-ω SST model fits in the literature and present experimental data, it was shown that the pressure distribution is not represented adequately by the model (Figure 11). Secondly, the transition SST and SAS models delay the drag coefficient fall at Re=40,000 of the k-ω SST model, but they all finally fall below the literature and actual experimental data at Re=140,000. The fall of the drag coefficient is a characteristic of the critical regimen (Re>140,000). Nevertheless, as it was analyzed in Figure 10, the turbulence models do not show the characteristics of the critical regimen, such as a boundary layer re-attachment. By the other side, the experimental drag coefficients obtained with the three-component balance show a better agreement than the simulations, with an underprediction of about 10%.

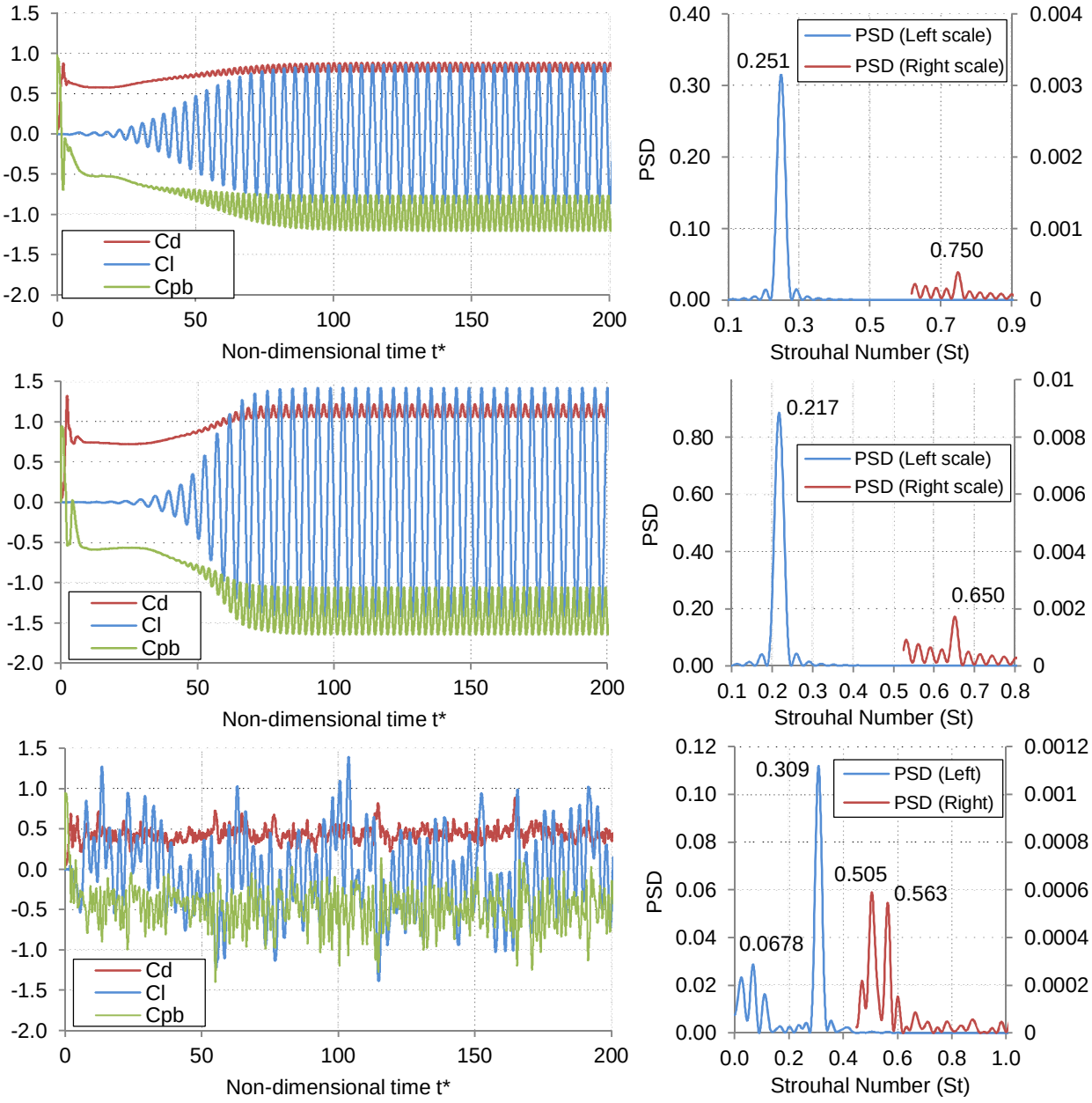

Figure 13. Time traces (left curves) and spectral analysis based on the lift coefficient with two scales (right curves) of k-ω SST (Upper), transition SST (Mid) and SAS models (Lower) for Re=140,000. Each time trace graph shows the time trace of C_D (upper red curve), C_L (mid blue curve) and C_{PB} (lower green curve).

The pressure suction coefficient in Figure 15 shows a good agreement between numerical results and literature experimental data for the laminar regimen, up to Re = 200. The transition SST and SAS models tend to delay the k-ω SST model pressure suction coefficient to fall at Re = 40,000. Re = 3,900 and 10,000 show the biggest discrepancies with experimental literature, with an error of around 120% for both cases. For Re = 40,000 and 140,000 large amplitudes are apparent, especially for the SAS models. On the other hand, the experimental measurements obtained in the wind tunnel underestimate the literature data in about 25% (Williamson, 1996).

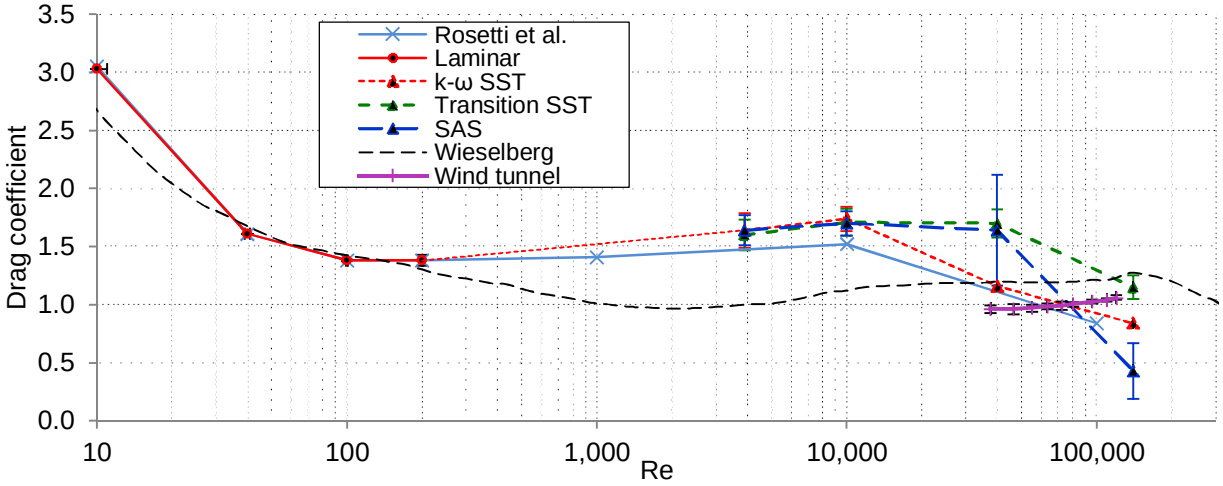

Figure 14. Drag coefficient (C_D) as a function of Reynolds number: (●) present work, with laminar viscous model; (---▲---) present work, k-ω SST turbulence model; (−−▲−−) present work, transition SST turbulence model; (▬▲▬) present work, SAS model; (−+−) present work, wind tunnel measurements; (−X−) numerical of Rosetti *et al.* (2012); (−−−) experiment of Wieselberg (Schlichting and Gersten, 2017).

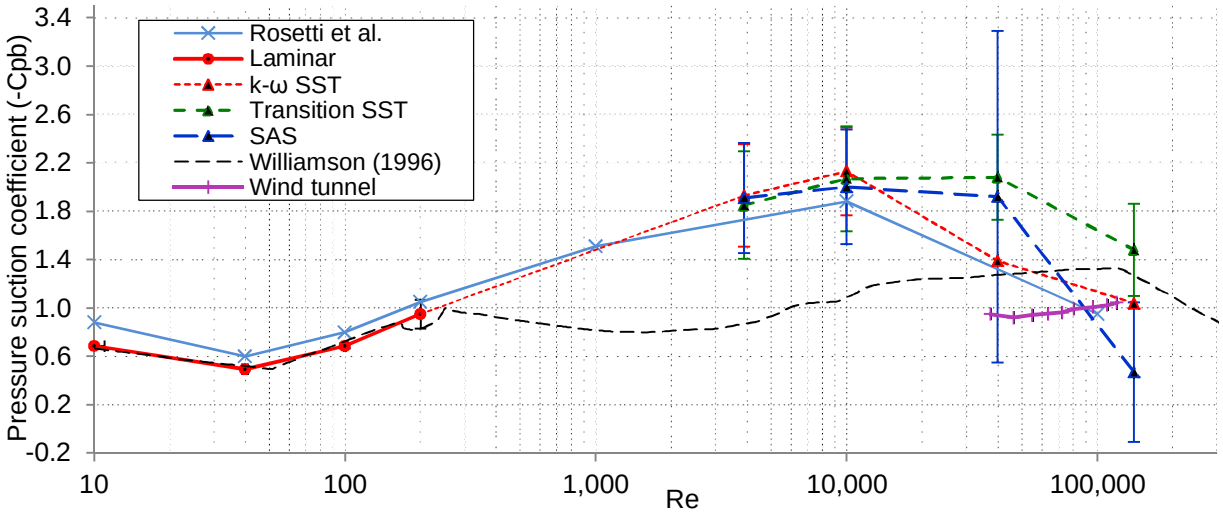

Figure 15. Base suction coefficient ($-C_{PB}$) as a function of Reynolds number: (●) present work, with laminar viscous model; (---▲---) present work, k-ω SST turbulence model; (−−▲−−) present work, transition SST turbulence model; (▬▲▬) present work, SAS model; (−+−) present work, wind tunnel measurements; (−X−) numerical of Rosetti *et al.* (2012); (−−−) experiment of Williamson (1996).

The Strouhal number was only calculated through numerical simulations. Notice how well the laminar Strouhal frequencies fit between the experimental measurements for rough and smooth cylinders (Lienhard, 1966). On the other hand, the numerical turbulence models overestimate the literature data over the smooth cylinder experimental curve. Nevertheless, a better agreement seems to appear for Re = 140,000, where the transition SST model fits in the experimental data and the SAS model seems to advance the experimental measurements for a smooth cylinder. Thus, experimentation and simulation taking into account the roughness of the cylinder at unsteady regimes seem to be an interesting topic to understand the vortex shedding behind the cylinder.

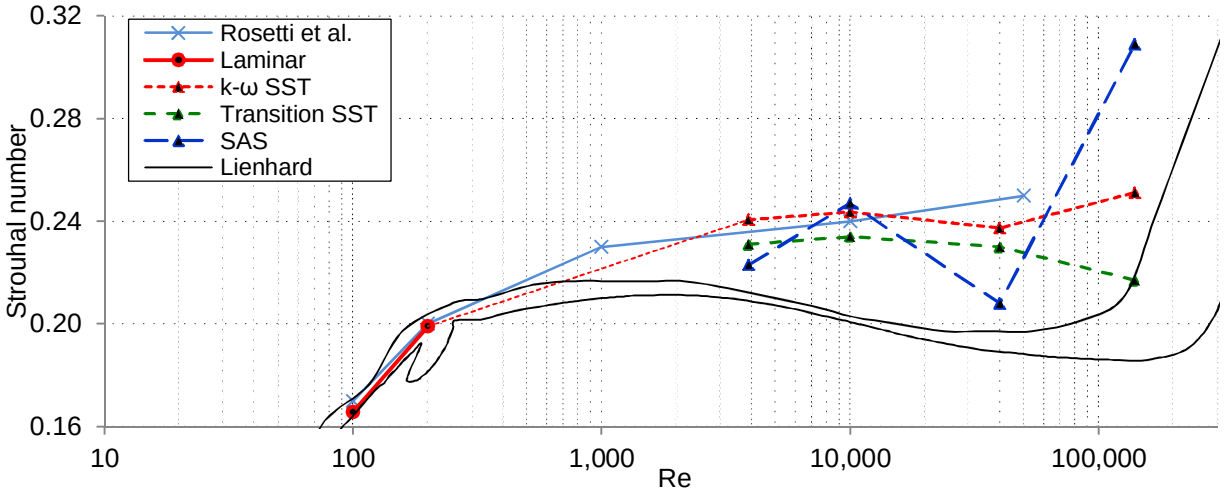

Figure 16. Strouhal number (St) as a function of Reynolds number: (●) present work, with laminar viscous model; (---▲---) k-ω SST turbulence model; (−−▲−−) transition SST turbulence model; (▬▲▬) SAS model; (−X−) Rosetti *et al*. (2012); (▬) compilation of Lienhard (1966) for Smooth cylinder (upper limit) and rough cylinder (lower limit).

The separation angle was measured in the wind tunnel by taking into account the inflection point of the pressure rise around the cylinder (Weidman, 1968). In this way, only two Reynolds numbers were considered, Re = 40,000 and Re = 100,000, from which good agreement with the literature is encountered. To obtain more accurate measurements in further investigations, skin friction measurement at the wall of the cylinder would be necessary. Once again, the laminar regime has a reasonable agreement with the numerical simulations and experimental literature. On the other hand, the turbulence models appear to overestimate the literature experimental data about 20 degrees for Re = 3,900 and 10,000. From the turbulence models used, the transition SST shows the best approach to experimental measurements for a Re=140,000.

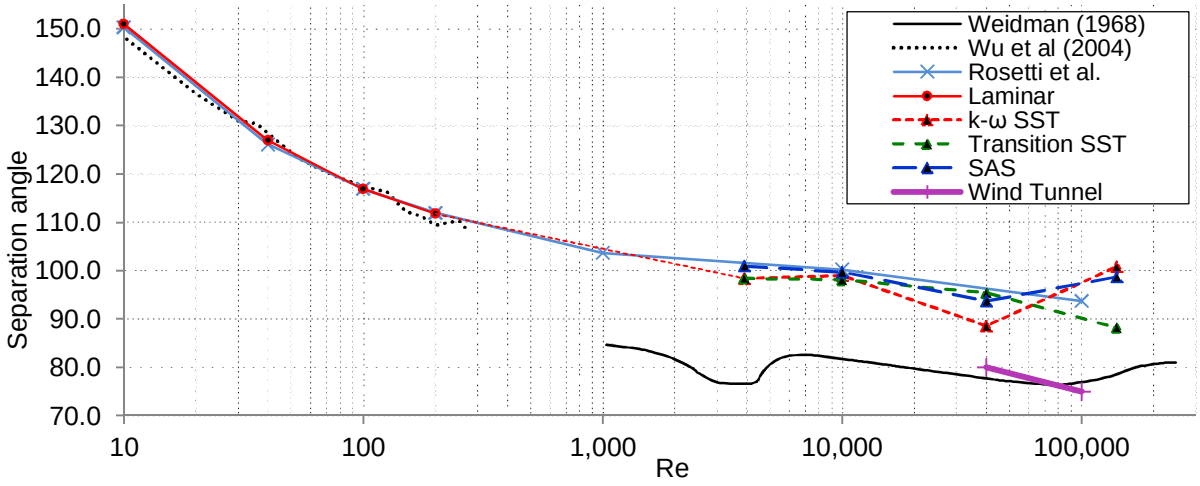

Figure 17. Separation angle (θ_S) as a function of Reynolds number. (●) present work with laminar viscous model; (---▲---) k-ω SST turbulence model; (−−▲−−) transition SST turbulence model; (▬▲▬)SAS model; (−X−) Rosetti *et al.* (2012); (▬) experiment of Weidman (1968) and (···) experimentof Wu et al. (2004)

5. CONCLUSIONS

A comparison between results obtained experimentally using a subsonic wind tunnel and numerically considering different turbulence models was carried out. It has been shown that our wind tunnel has the potential to carry out specialized research accounting for external flow. The results associated with velocities and pressures flow fields at the cylinder wall and wake, and the forces applied to the cylinder model, proved the capabilities of our wind tunnel and its current instrumentation to characterize external flows with enough precision. Nevertheless, different limitations were found in the spatial and temporal resolution of the available instrumentation. Thus, in the short term, an upgrade to

high-frequency hot-wire anemometry is considered a key aspect. This will provide a higher spatial and temporal resolution to the measurements carried out and allow capturing more properly transitional and turbulent effects.

In form of results, the different simulation strategies analyzed in this work showed that the computational cost can vary significantly (up to ten times), depending on the approach utilized. In addition, good agreement between this works numerical simulations and experimental data from the literature was found at laminar regimes. Although larger discrepancies were found at turbulent regimes, different avenues were left open to continue carrying out work on numerical approaches such as a three-dimensional analysis, SAS model considerations as a substitute to LES and an analysis of higher Reynolds numbers involving the critical and supercritical regimes. Qualitative agreement was achieved by comparing the results obtained from the numerical simulations and the wind tunnel experimental measurements, even though several numerical simplifications were introduced. In addition, the numerical simulations showed that regimes which the wind tunnel is not capable to reach, such as the laminar steady and unsteady regime, can be computed accurately.

Finally, as a comparison of experimental and numerical methods, it was noticed that perform variations of flow parameters, for instance, the Reynolds numbers can be simple using the experimental capabilities of the wind tunnel; nonetheless, data acquisition can be complicated in terms of instrumentation. On the other hand, the post-processing capabilities for numerical simulations are extensive; nevertheless, it can be limited to a specific flow regime defined by the Reynolds number or to a specific geometry model. Perform variations of the mentioned parameters in numerical simulations can demand high computational effort. Therefore, the complementary work between both methods, experimental and numerical, is of the utmost importance for the realization of more complex investigations.

6. ACKNOWLEDGEMENTS

The authors are particularly grateful to Alex A. Pachas Napa, member of the INACOM group of the PUCP, for the interesting discussions and advices concerning CFD, to Carlos Cabezas Chávez, supervisor of the LABEN of the PUCP, for his support in the experimental work, and to Sandra Tremolada Tovar for her extensive support and advising in the text formatting.

7. REFERENCES

Achenbach, E., 1968. "Distribution of local pressure and skin friction around a circular cylinder in cross-flow up to Re = $5x10^6$". *Journal of Fluid Mechanics*, Vol. 34(4), pp. 625–639.

Allen, H. J., and Vincenti, W. G., 1944. "Wall interference in a two-dimensional-flow wind tunnel, with consideration of the effect of compressibility". National Advisory Committee for Aeronautics [NACA], Report No. 782 (pp. 155–184). <https://ntrs.nasa.gov/archive/nasa/casi.ntrs.nasa.gov/19930091861.pdf>

ANSYS® Fluent, 2017a. *ANSYS® Fluent Theory Guide*, Release 18.2, help system.

ANSYS® Fluent, 2017b. *ANSYS® Fluent*, Release 19.0 [computer software]. <https://www.ansys.com/products/fluids/ansys-fluent>

ANSYS® ICEM CFD, 2017. *ANSYS® ICEM CFD*, Release 19.0 [computer software].

ANSYS® Workbench, 2017. *ANSYS® Workbench*, Release 19.0 [computer software]. <https://www.ansys.com/products/platform>

Braza, M., Chassaing, P., and Ha Minh, H., 1986. "Numerical study and physical analysis of the pressure and velocity fields in the near wake of a circular cylinder". *Journal of Fluid Mechanics*, Vol. 165, pp. 79–130

Cantwell, B. J., and Coles, D., 1983. "An experimental study of entrainment and transport in the turbulent near wake of a circular cylinder". *Journal of Fluid Mechanics*, Vol. 136, pp. 321-374.

Ferziger, J. H., and Peric, M., 2002. *Computational Methods for Fluid Dynamics*. Springer-Verlag, Berlin Heidelberg New York, 3rd edition.

Franke, J. and Frank, W., 2002. "Large eddy simulation of the flow past a circular cylinder at Re_D=3900". *Journal of Wind Engineering and Industrial Aerodynamics*, Vol. 90, pp. 1191–1206.

Hegner, F., Hess, D. and Brücker, C., 2015. "Volumetric 3D PIV in heart valve flow". In *11th International Symposium on Particle Image Velocimetry – PIV15*. Santa Barbara, California.

Jones, W. P., and Launder, B. E., 1972. "The prediction of laminarization with a two-equation model of turbulence". *International Journal of Heat and Mass Transfer*, Vol. 15(2), pp. 301–314.

Langtry, R. B., and Menter, F. R., 2009. "Correlation-Based Transition Modeling for Unstructured Parallelized Computational Fluid Dynamics Codes". *AIAA Journal*, Vol. 47(12), pp. 2894–2906.

Leipertz, A., and Sommer, R., 2009. "Time-resolved laser-induced incandescence". *Advances in Chemical Engineering*, Vol. 37, 223–269.

Libii, J. N., 2011. "Wind Tunnels in Engineering Education". In J. C. Lerner (Ed.), *Wind Tunnels and Experimental Fluid Dynamics Research*, Chap. 11. InTech, Rijeka.

Lienhard, J. J., 1966. "Synopsys of lift, drag, and vortex frequency data for rigid circular cylinders"

Lobasov, A. S., Chikishev, L. M., and Dulin, V. M., 2017. "Comparison between premixed and partially premixed combustion in swirling jet from PIV, OH PLIF and HCHO PLIF measurements". In *Journal of Physics: Conference Series*. Vol. 899.

Menter, F. R. and Egorov Y., 2010. "The scale-adaptive simulation method for unsteady turbulent flow predictions. part 1: Theory and model description". *Flow, Turbulence and Combustion*, Vol. 85(1), pp. 113–138.

Menter, F. R., 1994. "Two-equation eddy-viscosity turbulence models for engineering applications". *AIAA Journal*, Vol. 32(8), pp. 1598–1605.

Menter, F. R., Kuntz, M., and Langtry, R., 2003. "Ten Years of Industrial Experience with the SST Turbulence Model". *Turbulence, Heat and Mass Transfer 4*.

Menter, F. R., Langtry, R. B., Likki, S. R., Suzen, Y. B., Huang, P. G., and Völker, S., 2006. "A Correlation-Based Transition Model Using Local Variables—Part I: Model Formulation". *Journal of Turbomachinery*, Vol. 128(3), pp. 413 - 422.

Molki, A., Khezzar, L., and Goharzadeh, A., 2013. "Measurement of fluid velocity development in laminar pipe flow using laser Doppler velocimetry". *European Journal of Physics*, Vol. 34(5), pp. 1127–1134.

Norberg, C., 2003. "Fluctuating lift on a circular cylinder: Review and new measurements". *Journal of Fluids and Structures*, Vol. 17(1), pp. 57–96.

Palkin, E., Mullyadzhanov, R., Hadžiabdić, M., and Hanjalić, K., 2016. "Scrutinizing URANS in Shedding Flows: The Case of Cylinder in Cross-Flow in the Subcritical Regime". *Flow, Turbulence and Combustion*, Vol. 97.

Parnaudeau, P., Carlier, J., Heitz, D., and Lamballais, E., 2008. "Experimental and numerical studies of the flow over a circular cylinder at Reynolds number 3900". *Physics of Fluids*, Vol. 20(8).

Pereira, F. S., Vaz, G., Eça, L., and Girimaji, S. S., 2015. "Flow Past a Circular Cylinder: A Comparison Between RANS and Hybrid Turbulence Models for a Low Reynolds Number". In *Proceedings of ASME 34th International Conference on Ocean, Offshore and Arctic Engineering - OMAE 2015*. St. John's, Canada.

Pereira, F. S., Vaz, G., Eça, L., and Girimaji, S. S., 2018. "Simulation of the flow around a circular cylinder at Re=3900 with Partially-Averaged Navier-Stokes equations". *International Journal of Heat and Fluid Flow*, Vol. 69.

Raghavan, K., and Bernitsas, M. M., 2011. "Experimental investigation of Reynolds number effect on vortex induced vibration of rigid circular cylinder on elastic supports". *Ocean Engineering*, vol. 38, pp. 719–731.

Ristić, S., 2007. "Flow Visualisation Techniques in Wind Tunnels Part I – Non optical Methods". *Scientific Technical Review*, Vol. LVII(1), 39–50.

Rosetti, G. F., Vaz, G., and Fujarra, A. L. C., 2012. "URANS Calculations for Smooth Circular Cylinder Flow in a Wide Range of Reynolds Numbers: Solution Verification and Validation". *Journal of Fluids Engineering*, Vol. 134.

Roshko, A., 1961. "Experiments on the flow past a circular cylinder at very high Reynolds number". *Journal of Fluid Mechanics*, Vol. 10, pp. 345–356.

Schlichting, H. and Gersten, K., 2017. "Some Features of Viscous Flows". In H. Schlichting (Deceased) and K. Gersten, *Boundary Layer Theory*, chap. 1. Springer-Verlag, Heidelberg.

Stringer, R. M., Zang, J. and Hillis, A. J., 2014. "Unsteady RANS computations of flow around a circular cylinder for a wide range of Reynolds numbers". *Ocean Engineering*, Vol. 87.

TecQuipment, 2017. VDAS® Versatile Data Acquisition Software. Version: 2.7.0.16611 [computer software] <https://www.tecquipment.com/es/vdas>

Tritton, D. J., 1988/2007, *Physical Fluid Dynamics*. Oxford University Press Inc., New York, 2nd edition.

Weidman, P. D., 1968. *Wake transition and blockage effects on cylinder base pressures*. Degree thesis, California Institute of Technology, Pasadena, California.

Wilcox, D. C., 1988. "Reassessment of the Scale-Determining Equation for Advanced Turbulence Models". AIAA Journal, Vol. 26(11), pp. 1299–1310.

Williamson, C. H. K., 1996. "Vortex Dynamics in the Cylinder Wake". *Annual Review of Fluid Mechanics*, Vol. 28, pp. 477–539.

Wu, M-H., Wen, C-Y., Yen, R-H., Weng, M-C. and Wang, A-B., 2004. "Experimental and numerical study of the separation angle for flow around a circular cylinder at low Reynolds number". *Journal of Fluid Mechanics*, Vol. 515, pp. 233–260.

Young, M., and Ooi, A., 2007. "Comparative Assessment of LES and URANS for Flow Over a Cylinder at a Reynolds Number of 3900". In *16th Australasian Fluid Mechanics Conference*. Gold Coast, Australia.

Zdravkovich, M. M., 1990. "Conceptual overview of laminar and turbulent flows past smooth and rough circular cylinders". *Journal of Wind Engineering and Industrial Aerodynamics*, Vol. 33, pp. 53–62.Achenbach, E. (1968). Distribution of local pressure and skin friction around a circular cylinder in cross-flow up to Re = 5:106. *Journal of Fluid Mechanics*, *34*(4), 625–639.

8. RESPONSIBILITY NOTICE

The authors are the only responsible for the printed material included in this paper.